# A COMPARISON OF BEAM-INDUCED DAMAGE FROM XENON AND GALLIUM FOCUSED ION BEAMS

By SAMUEL R. NORRIS, B.S.

Thesis Submitted to the School of Graduate Studies in Partial Fulfillment of the Degree Master of Applied Science

McMaster University © Copyright by Samuel Norris, 2019

McMaster University, Hamilton Ontario

MASTER OF APPLIED SCIENCE (2019), Materials Science and Engineering

TITLE: A Comparison of Beam-Induced Damage from Xenon and Gallium Focused Ion Beams

AUTHOR: Samuel Norris, B.S. (Centre College)

SUPERVISOR: Nabil D. Bassim

NUMBER OF PAGES: xii, 43

## LAY ABSTRACT

The second half of the 20th century saw the advent of nanotechnology, both in the context of understanding the structure of the natural world beyond the limit of light microscopy, as well as manipulating materials to create useful microscopic devices, including the computers ubiquitous in today’s life. One technology that has contributed to today’s nano-centric paradigm is the focused ion beam/scanning electron microscope (FIB/SEM). The FIB/SEM is used to machine materials with extreme precision for many diverse applications such as modifying microcircuits, three-dimensional (3D) nanotomography, or to prepare samples for other microscopy techniques. For some applications, however, damage to the sample from the ion beam can be fatal. New ion sources have become available in the past ten years that may cause less damage to samples, and thus open up new applications for FIB. This thesis includes first a description of a series of optical devices prototyped using FIB. This is followed by a comparison of the damage induced by the conventional liquid gallium ion source and new xenon plasma ion sources, and a discussion of the relative merits of the ion sources for optical device fabrication.

# ABSTRACT

Focused ion beam/scanning electron microscopy (FIB/SEM) is a tool commonly used for applications including preparation of site-specific transmission electron microscopy (TEM) samples, nanotomography, and electronic circuit edit. Another potential application is optical device prototyping; however, the ion beam itself has been shown to cause damage fatal to device operation. This thesis first includes several examples of FIB-fabricated optical devices that had limited functionality compared to simulation. Second, the underlying causes of ion beam-induced optical damage from gallium and xenon ion sources is characterized.

Monte Carlo simulations of ion-solid interactions were confirmed using TEM analysis to measure the thickness of the damaged layer. For crystalline samples such as silicon, Raman response can be used as a measure of lattice damage. Using these techniques, it was found that optical damage from a gallium beam is more severe than from a xenon beam, and occurs in the form of lattice amorphization and implantation of beam ions. This damage hinders optical coupling by altering the physical and electronic structure of the sample. Consequently, the xenon PFIB is a better choice for optical device prototyping.

# ACKNOWLEDGEMENTS

*I first would like to thank my advisor, Dr. Nabil Bassim, for making my master's studies possible, and for opening many doors for me. It was an impromptu suggestion that led me to McMaster, and although nothing is perfect, "this is the life we have chosen", and I think coming here has been a great experience.*

*I would like to thank Keana Scott for setting me on the path of research generally, and electron microscopy specifically. Your trust in me when I was at NIST instilled a confidence that has helped me immeasurably. I will always value your advice, and I'm looking forward to collaborating again in the future.*

*I would like to thank my comrades in the Bassim group for exposing me to so many new scientific ideas, new cultures, and the experiences that made my stay in Canada unique. The students, staff, and faculty of the Materials department the CCEM welcomed me to the program and often helped me beyond what I deserve, and I appreciate it.*

*Finally, I would like to thank my sisters and parents for helping to maintain my sanity and health through the long dark winters when my edges began to fray.*

# Table of Contents

LAY ABSTRACT ..... iii
ABSTRACT ..... iv
ACKNOWLEDGEMENTS ..... v
LIST OF ABBREVIATIONS ..... viii
LIST OF FIGURES ..... x
LIST OF TABLES ..... xii
DECLARATION OF ACADEMIC ACHIEVEMENT ..... xii
CHAPTER 1: INTRODUCTION ..... 1
1.1 Focused Ion Beam - History ..... 1
1.2 Ion Beam Damage: a Barrier to Wider FIB Applications ..... 2
1.3 Research Objectives ..... 3
CHAPTER 2: LITERATURE REVIEW ..... 5
2.1 Ion Sources ..... 5
2.2 FIB applications ..... 10
2.2.1 Circuit Edit and Mask Repair ..... 10
2.2.2 Sample Preparation ..... 11
2.2.3 Nanotomography ..... 13
2.2.4 Photonic Device Fabrication ..... 14
2.3 Ion Beam Damage ..... 15
2.4 Characterization techniques ..... 18
2.4.1 Transmission electron microscopy/electron energy loss spectroscopy ..... 18
2.4.2 Raman Spectroscopy ..... 19
CHAPTER 3: EXPERIMENTS AND METHODS ..... 23
3.1 PHOTONIC DEVice Fabrication ..... 23
3.1.1 Waveguide End Facets ..... 23
3.1.2 DFB Laser ..... 25
3.1.3 IR Polarizer ..... 27
3.2 Beam damage ..... 29
3.2.1 TEM/EELS ..... 30
3.2.3 Raman Spectroscopy ..... 32
CHAPTER 4: RESULTS AND DISCUSSION ..... 34
CHAPTER 5: CONCLUSIONS ..... 41

5.1: Future Work ..... 42
REFERENCES ..... 43

# LIST OF ABBREVIATIONS

ADF – Annular darkfield

BCA – Binary collision approximation

CMOS – Complementary metal oxide semiconductor

CT – Computed tomography

DFB – Distributed feedback

DBR – Distributed Bragg reflector

EBL – Electron beam lithography

EBSD – Electron backscatter diffraction

EDS – Energy dispersive x-ray spectroscopy

EELS – Electron energy loss spectroscopy

FIB – Focused ion beam

FIM – Field ion microscope

GIS – Gas injection system

HAADF – High-angle annular darkfield

hBN – Hexagonal boron nitride

ICP – Inductively coupled plasma

IR – Infrared

LMIS – Liquid metal ion source

MEMS – Microelectromechanical systems

PFIB – Plasma focused ion beam

PIC – Photonic integrated circuit

RF – Radio frequency

ROI – Region of interest

SBE – Surface Binding Energy

SE – Secondary electron

SEM – Scanning electron microscopy

SOI – Silicon on Insulator

SMF – Single mode fiber

SRIM – Stopping and range of ions in matter

TEM – Transmission electron microscopy

TO – Transverse optical

TA – Transverse acoustic

UV - Ultraviolet

ZLP – Zero loss peak

# LIST OF FIGURES

Figure 1.1: Modern dualbeam FIB/SEM at McMaster University

Figure 1.2: SRIM Collision cascade of a single 30 kV gallium ion into silicon nitride. Paths of displaced silicon atoms in yellow, paths of displaced nitrogen atoms in blue

Figure 2.1: Field ion micrograph of a sharp Pt tip (From Muller)

Figure 2.2: Gallium Liquid Metal Ion Source (Courtesy ThermoFisher)

Figure 2.3: Schematic of inductively coupled plasma ion source (From Smith et al)

Figure 2.4: Photomask repair by FIB (From Melngailis et Al)

Figure 2.5: Steps of the FIB liftout process: a) Protective metal cap, b) rough trench cuts, c) micromanipulator lifting lamella from bulk, d) welding lamella to TEM grid e) thinning lamella to electron transparency

Figure 2.6: Stages of Atom Probe Sample Preparation with FIB (From Larson, Foord Et Al.)

Figure 2.7: Schematic of typical FIB tomography setup

Figure 2.8: FIB-fabricated photonic crystal (From Balasaubramanian et al)

Figure 2.9: Simulation of Primary beam ion trajectories in silicon Top) Normal incidence, mean range of 27.9 nm. Bottom) 88° angle of incidence, mean range of 8.0 nm.

Figure 2.10: Schematic of EELS instrumentation (Courtesy Gatan)

Figure 2.11: Rayleigh vs. Raman Scattering

Figure 2.12: Raman spectrum of single-crystal silicon

Figure 2.13: Raman spectrum of single-crystal and amorphous silicon (Courtesy ThermoFisher)

Figure 3.1: Left) Edge facet of an SOI chip as diced. right) FIB-processed waveguide facets

Figure 3.2: SEM micrograph of an indium phosphide Amplifier before FIB-milling of Bragg grating

Figure 3.3: Schematic of distributed Bragg reflector

Figure 3.4: Distributed Bragg reflector, 241 nm pitch

Figure 3.5: Optical power output of DFB laser

Figure 3.6: Lattice structure of a van der Waals crystal

Figure 3.7: SEM Micrograph of IR polarizer device in hBN

Figure 3.8: E-beam deposited carbon on 10 kV gallium-irradiated surface

Figure 3.9: (Inset) 30 kV gallium-irradiated surface and resulting TEM sample

Figure 3.10: Example of dose array for damage characterization by Raman

Figure 4.1: ADF images of ion beam damage. Top left) 30 kV gallium, top right) 10 kV gallium, bottom left) 30kV xenon, bottom right) 5 kV xenon

Figure 4.2: SRIM simulations of ion range. Top Left) gallium 30 kV Top Right) gallium 10 kV Bottom left) xenon 30 kV Bottom right) xenon 5 kV

Figure 4.3: Gallium segregation at Low dose. Left) 10 kV, Right) 30 kV

Figure 4.4: ADF image and EELS maps of high-dose, 30 kV-irradiated samples Top) Gallium, Bottom) Xenon

Figure 4.5: Raman Spectra of gallium and xenon exposed silicon

Figure 1: Raman Intensity vs ion dose for Ga and Xe FIB (30 kV)

# LIST OF TABLES

Table 2.1: Brightness and energy spreads from various ion sources (From Smith et al)

Table 3.1: Loss measurements before and after FIB-faceting

Table 4.1: Measured amorphous layer thicknesses

# DECLARATION OF ACADEMIC ACHIEVEMENT

I hereby declare to be the sole author of this document and note that the research work presented in this thesis was primarily completed by myself, with some contribution from the following people:

- Design and simulation for IR polarizer devices, and hBN material was provided by Tom Folland at Vanderbilt University, Department of Mechanical Engineering
- Waveguides and optical amplifier samples, as well as optical measurements were provided by the Bradley and Knights groups at McMaster University, Department of Engineering Physics
- Assistance with EELS spectroscopy was provided by Natalie Hamada at the Canadian Center for Electron Microscopy

All TEM and FIB/SEM microscopy was completed at the Canadian Center for Electron Microscopy (CCEM) at McMaster University, Hamilton, Ontario. Raman spectroscopy was completed in the Adronov lab at McMaster University, Hamilton, Ontario.

# CHAPTER 1: INTRODUCTION

## 1.1 FOCUSED ION BEAM - HISTORY

Commercial focused ion beam instruments were first developed in the 1980's as a tool to repair photomasks for the microprocessor manufacturing industry. The first major review paper dedicated to focused ion beam technology was published in 1987 by John Melngailis. In his abstract, he estimated the total number of focused ion beam systems in the world at about 35, mostly in Japan (Melngailis, 1987). In 1993, FEI Company (recently acquired by ThermoFisher Scientific) released the first commercial gallium FIB integrated with a scanning electron microscope (SEM) column in a dual-beam configuration (Williams, 2014). Today, there are thousands of dual-beam FIB/SEMs (all references to "FIB" in this thesis refer to dual-beam instruments) in industry and research laboratories around the world. This explosion has resulted from vast improvement in instrument capabilities and ease-of-use. Current applications (which will be discussed at length in the next chapter) have expanded beyond the semiconductor industry to include resistless direct-write lithography of photonic devices, transmission electron microscope (TEM) and atom-probe tomography (APT) sample preparation, and nanotomography by serial sectioning. FIB is a critical tool for each of these applications due to its direct-writing resolution, site-specificity, and versatility across many material systems.

## 1.2 ION BEAM DAMAGE: A BARRIER TO WIDER FIB APPLICATIONS

Sputtering, or the removal of surface atoms due to transfer of kinetic energy from the primary beam, is an inexact process. As with electrons in an SEM, many different interactions between sample and beam are possible. Only a portion of the energy in the incident beam is dissipated as the kinetic energy of sputtered particles. Other energy is transferred to phonons: collective vibrations of the nuclei in a lattice. Phonons dissipate energy as heat in the bulk of a material. Most of the remaining beam energy goes into the creation of dislocations or rearrangement of the atoms of the sample through collisions with the nuclei of the sample surface. If the energy is greater than the surface binding energy (SBE), material is ejected, either as a neutral atom, ion, or cluster of atoms (Kudriavtsev, Villegas, Godines, & Asomoza, 2005). When an ion is incident on the surface, the first inelastic collision may transfer enough energy to a sample atom for it to dislocate another ion in turn, and so on for many atoms until there is not enough energy left, and the dislocations stop. This is known as a collision cascade within the sample.

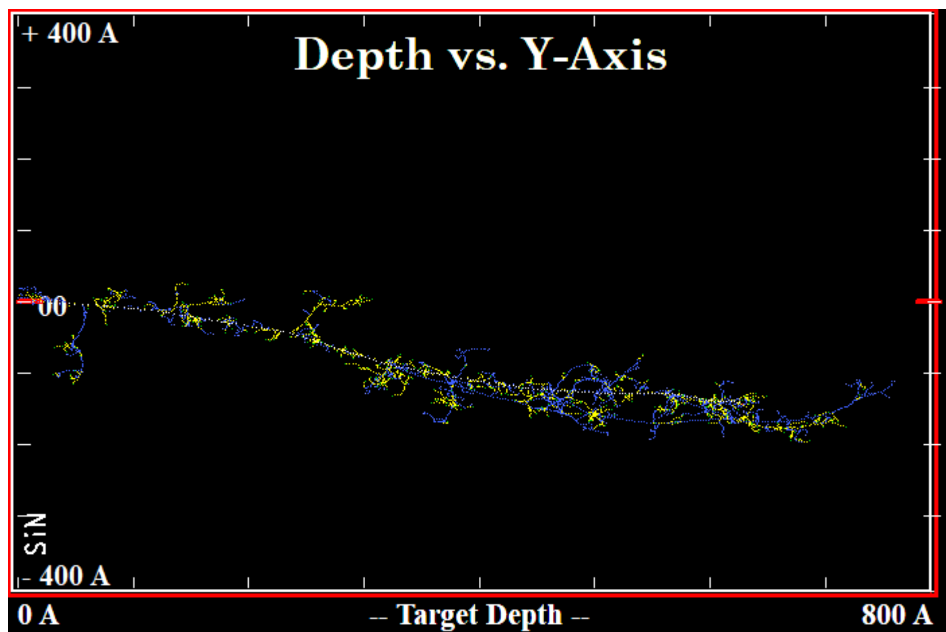


FIGURE 1.2: SRIM COLLISION CASCADE OF A SINGLE 30 KV GALLIUM ION INTO SILICON NITRIDE. PATHS OF DISPLACED SILICON ATOMS IN YELLOW, PATHS OF DISPLACED NITROGEN ATOMS IN BLUE.

With many ions, the surface is completely amorphized to the depth of the cascade. Additionally, some of the incident beam ions are trapped, or implanted, in the sample. The process of intentionally implanting of heteroatoms is known as doping. The concentration and implant depth are controlled by tuning beam

current and accelerating voltage. Doping is ubiquitous in semiconductor processing to alter the electronic properties of a crystal.

Both the amorphization of the lattice and implantation of beam ions are considered damage, since they alter the structure and chemistry of the original material. Accordingly, this damage can have a major effect on electronic and optical properties, generally reducing the possible efficiency of FIB-fabricated devices. With the gallium liquid metal ion source (LMIS), implantation is particularly problematic since gallium can alloy with metals such as aluminum and change the stoichiometry of some common semiconductors such as gallium arsenide (Belz, Beyer, Torunski, Stolz, & Volz, 2016). To overcome these challenges, other ion source technologies are being tested as alternatives to gallium. One source that has recently become commercially available is based on an inductively coupled plasma (ICP), using xenon gas as the source of ions. An instrument equipped with the xenon ICP source is known as a plasma-FIB (PFIB). Xenon ions from the ICP source exhibit both reduced amorphous layer thickness and less chemical effects than the gallium LMIS (Burnett et al., 2016). Lithographic applications that have been impossible due to gallium implantation and damage in LMIS-based FIBs may now be achievable using the new ion source.

## 1.3 RESEARCH OBJECTIVES

FIB milling has the potential to advance fields such as photonics, microelectromechanical systems (MEMS), and biomaterials by enabling rapid prototyping of complex three-dimensional structures. Additionally, it will continue to be an indispensable tool for sample preparation for ever more demanding characterization tasks. A central stumbling block, however, is damage introduced by the beam itself. As new ion sources emerge and are developed into commercial instruments, greater understanding of beam damage is needed to fully utilize the unique characteristics of different ion sources.

The research presented in this thesis falls into two general sections – photonic device fabrication and characterization of ion beam damage, with the following objectives:

- To fabricate novel photonic devices that are difficult or impossible to make using conventional fabrication techniques
- To experimentally compare the damage caused by xenon and gallium ions in order to evaluate the effects of beam damage on the performance of above devices. Experiments will use TEM

and electron energy loss spectroscopy to measure damage depth and ion implantation, as well as Raman spectroscopy to measure optical coupling.

# CHAPTER 2: LITERATURE REVIEW

## 2.1 ION SOURCES

Since the 1950s, diverse efforts have been made to develop stable, high-current sources of various species of ion. The controlled generation of positively charged particles has had many applications other than FIB, including mass spectrometry and spacecraft propulsion (Fenn, Mann, Meng, Wong, & Whitehouse, 1989; Uberoi, 1964). One of the first ion sources came from the field ion microscope (FIM), a surface analytical technique capable of atomic resolution imaging (Müller & Bahadur, 1956). In the FIM, a sharp metal needle with a radius under 100 nm (the sample) is placed at a high bias. Due to the curvature and radius of the electrode, the electric field gradient at the tip is high enough to cause an electron to tunnel from an "imaging" gas atom into the tip. Once the gas (generally hydrogen, helium, or neon) is ionized, it is accelerated towards a phosphor screen. Bright spots on the screen represent the location of the atoms on the electrode tip (where ionization took place).

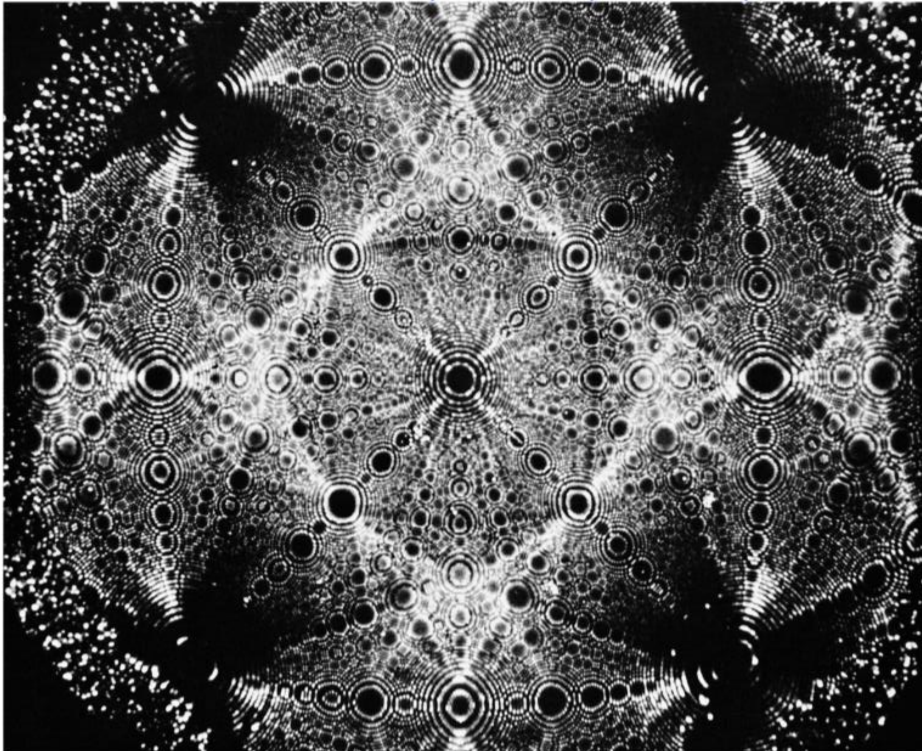

**FIGURE 2.1: FIELD ION MICROGRAPH OF A SHARP PT TIP (FROM MULLER 1956)**

This principle is the basis of the modern instrument known as the atom probe, in which the metal tip is ionized one atom at a time, causing a steady stream of ion to be emitted from the source. Field ionization has recently been adapted into a gas field ionization source (GFIS), now available in the commercial helium ion microscope. However, while the GFIS has a small virtual source and is capable of

extremely small beam diameters and high-resolution imaging, the total emission current is quite low, and it cannot provide enough current to be a micromachining tool in most cases (Economou, Notte, & Thompson, 2012). To be useful for micromachining, an ion source needs the following characteristics: high brightness, low energy spread, and high current. The brightness *B* of an ion source is defined as the emitted current *I* divided by the area *A* and solid angle *Ω* into which ions are emitted.

$$B = \frac{I}{A * \Omega}$$

In units of $Am^{-2}sr^{-1}$. Since the angle into which ions are emitted changes at different emission voltages, a more useful metric is reduced brightness β, where *B* is brightness as calculated above and *V* is the emission voltage:

$$\beta = \frac{B}{V}$$

Reduced brightness is a critical metric when describing ions sources because it (along with energy spread) determines both the highest current at a given spot size and the finest possible beam at any current. A high brightness means that sufficient current to be extracted from a very small virtual source, and the small source allows for a small crossover diameter and hence ultimate focusability (Komuro, Kanayama, Hiroshima, & Tanoue, 1983). The typical brightness of Xe ICP, gallium LMIS, and He GFIS sources are approximately $10^4$, $10^6$, and $10^9$ $Am^{-2}sr^{-1}V^{-1}$ respectively. While Xe does have a lower brightness than the other sources, the ICP has a higher angular intensity due to the larger area of emission, which allows finer beams at higher currents (above 100 nA).

TABLE 2.1: BRIGHTNESS, ENERGY SPREAD, AND CURRENT RANGE FOR VARIOUS ION SOURCES (ADAPTED FROM SMITH ET AL, 2014)

| Ion Species | $\beta_r$ ($Am^{-2}sr^{-1}V^{-1}$) | $\Delta E_{FWHM}$ (eV) | Beam Current Range |
|---|---|---|---|
| $Xe^+$ (ICP) | 1 x $10^4$ | 5 | 0.1 pA to 10 µA |
| $O^-$ (ICP) | 4 x $10^2$ | 3.5 | 0.1 pA to 400 nA |
| $He^+$ (GFIS) | 1 x $10^9$ | 1 | 0.1 pA to 10 pA |
| $Ga^+$ (LMIS) | 1 x $10^6$ | 5 | 0.2 pA to 50 nA |

The energy spread of emitted ions determines the degree of chromatic aberration suffered in the optical system, since particles of different energies experience the electric field of the focusing lenses differently. The largest contributor to energy spreading is thermal energy in ions prior to

acceleration. In the LMIS, which operates above room temperature, this is about 5 eV (Forbest, 1997). The ICP source has a similar spread of energy due to ionization occurring at different locations in the chamber with different field gradients. However, at least 2 eV of the spread in the ICP is due to temporal fluctuations of the radio frequency (RF) current (N. S. Smith, Tesch, Martin, & Kinion, 2008). If this can be eliminated, the resolution of the PFIB could be increased significantly.

### 2.1.1 GALLIUM LMIS

In the mid-20th century, pioneers of the nascent field of space exploration were considering many methods of accelerating a massive body through space without an atmosphere. One proposed method at the time (and still an active area of research to this day) was to accelerate a beam of small but heavy particles behind a craft to provide acceleration and directional control. The principle of the LMIS was tested with many elements and compounds, particularly metals and eutectic alloys with low melting points and a high mass to ionization energy ratio. Recently, a cesium-based LMIS has become available off the shelf as an attitude-control thruster for small satellites (CubeSatShop, 2019).

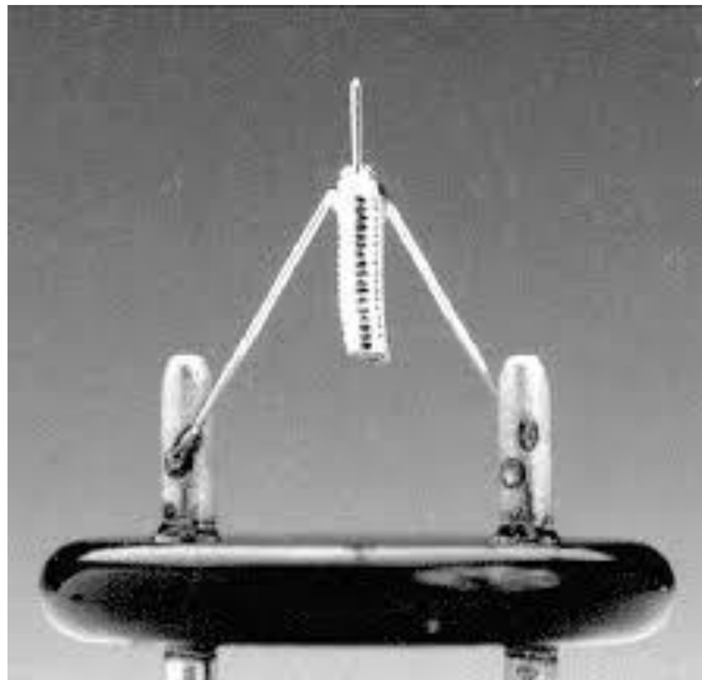

**FIGURE 2.2: GALLIUM LIQUID METAL ION SOURCE (COURTESY THERMOFISHER)**

Instruments that require high focusability (such as a FIB or ion microscope) require either a highly pure elemental source material, or an additional component called a Wein filter. The Wein (or E x B) filter selects a specific mass to charge ratio, which enables both selection of a single ion species (in the case of compound sources) and elimination of multiply charged ions (Wang, Ward, & Seliger, 1981).

While commercial FIB systems have been made around alloy sources, the added cost and complexity of the Wein filter has relegated it to niche applications. Gallium was found to be the most suitable general-purpose LMIS material; it has low volatility, low melting point, high atomic mass (and sputter yield), and is relatively easy to ionize singly. Therefore, the vast majority of FIB/SEM systems in use today utilize the gallium LMIS source.

The LMIS (as it is used in FIB) consists of a sharp tungsten needle (tip radius under 1 µm) wetted by liquid gallium supplied from a reservoir behind the tip. During operation, the needle is biased against an "extractor" electrode such that electrostatic forces force the liquid gallium into a fine cone (approximated by Taylor's theory to 49.3°) with a tip radius of roughly 5 nm. The fine tip enables an electric field gradient of 2 V/Å, sufficient to cause field evaporation (Swanson, 1983). Once gallium ions are ejected from the tip of the Taylor cone, they enter the optical system of the ion column. While the virtual source size of the gallium LMIS is found to be on the order of a nanometer or less (by back-tracing the trajectories of ejected ions), it is unfortunately impossible to maintain a spot size on the sample on the same scale. This is due to the relatively large energy spread of ejected ions: over 5 eV. This spread causes chromatic aberration in ion optical systems, limiting the spot size on the sample to about 5 nm despite the virtual source size within the LMIS tip (calculated by back-tracing ions) being under 1 nm.

The current through the source tip must be at least 0.5 µA to maintain stability of the cone, but the energy spread of emitted ions increases at higher currents, so most LMISs operate at 1-2 µA (Orloff, 1993). However, much of this current is emitted at angles far from the optical axis and is thus unsuitable for a finely focused beam. Another electrode known as a suppressor is used to reject these ions. This limits the down-column current to around 100 nA to maintain the high angular brightness of the source. While the gallium LMIS is a versatile and practical ion source, it does have several major limitations such as the limited beam current, as well as chemical effects from the gallium itself.

### 2.1.2 XENON PLASMA

A fundamentally different ion source technology, inductively coupled plasma (ICP), was developed in the 2000s to overcome these limitations. Xenon PFIBs became available from several manufacturers in the early 2010s.

The ICP source consists of a sealed chamber surrounded by an RF coil. Low-pressure xenon gas is flowed into the chamber. Current is passed through the coil at a frequency below the electron plasma

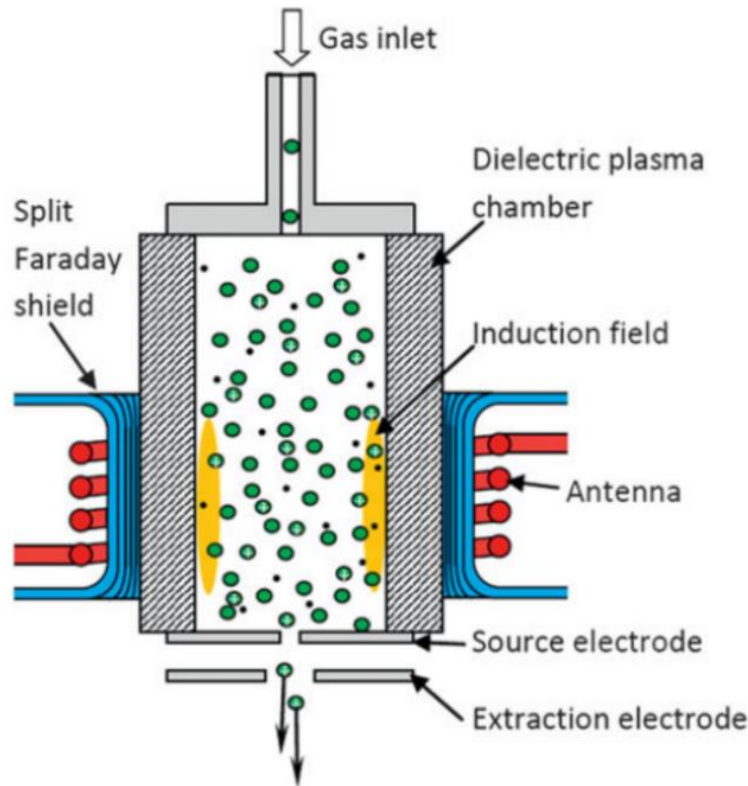


FIGURE 2.3: SCHEMATIC OF INDUCTIVELY COUPLED PLASMA ION SOURCE (FROM SMITH ET AL 2014)

frequency accelerating plasma electrons in the induction field at the edges of the chamber without heating the xenon ions, which is critical for minimizing energy spread, and hence chromatic dispersion. The skin layer of energetic electrons gains enough kinetic energy to in turn ionize xenon atoms, which are then extracted. The rate of generation is dependent on the power in the RF coil and the flow rate of feed gas into the chamber. Ions are then accelerated by a series of extractor optics and focused down the column. Since the source in an ICP system is an area, as opposed to a point source in the LMIS, the absolute brightness at low currents is lower than in a gallium FIB, and the smallest spot size attainable is commensurately larger (a rigorous examination of the highest imaging resolution currently possible with a xenon ICP source was not found in the literature, but is on the order of 10 nm).

The most apparent advantage of the PFIB is the high beam currents that are possible. While the source brightness is lower than that of the gallium LMIS, the angular spread is much lower as well. This means that more of the ions generated are focused down the column: the PFIB can operate at currents up to 2.5 µA. This allows milling up to two orders of magnitude faster than is possible in the gallium FIB. Additionally, the different ion species results in different ion-solid interactions such as lattice amorphization in crystalline samples and ion implantation.

## 2.2 FIB APPLICATIONS

Although it was originally a niche tool in the semiconductor industry, today FIB is used across any field of science and engineering that requires high-resolution analysis or manipulation of materials. This section will detail the applications of FIB instruments from conventional to cutting edge.

### 2.2.1 CIRCUIT EDIT AND MASK REPAIR

The first widespread use of the FIB came from the burgeoning microelectronics industry in the 1970s and 80s. When a macro-scale circuit fails, it can be repaired or modified by cutting a wire or attaching a new one to bypass the problem. As the feature size on integrated circuits continued to shrink and devices became increasingly integrated and complex, it became impossible to modify circuits using conventional tools. The first FIBs did not have an electron column but were able to image (albeit at relatively low resolution) using ion-induced secondary electron (SE) emission. This era also saw the use of various gas chemistries to enhance etching rates and for material deposition. The combined ability to locate features, remove material, and deposit insulators and conductors in the same chamber allowed, for the first time, modification of a microcircuit (Harriott, Wagner, & Fritz, 1986). Alongside the miniaturization of microelectronics came an increase in the sophistication of photolithography masks. Both types of defects in ultraviolet (UV) and X-ray masks (locations that are either transparent and should be opaque or vice versa) can be repaired by FIB: deposition to optically occlude an area or etching to remove the opaque layer (Atwood, Fisanick, Johnson, & Wagner, 1984).

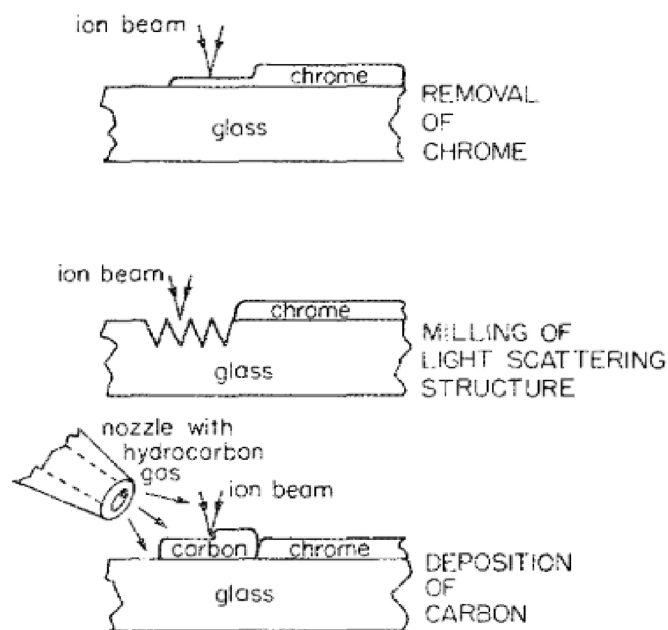


**FIGURE 2.4: PHOTOMASK REPAIR BY FIB (FROM MELNGAILIS ET AL 1987)**

### 2.2.2 Sample Preparation

Probably the most ubiquitous use of FIB today both in and out of the semiconductor industry is the preparation of TEM and APT samples. The first publication documenting the preparation of a TEM sample using FIB is from 1993, with the authors extracting a sample of silicon 10 x 5 x 0.2 µm in size (Overwijk, Heuvel, & Bulle-Lieuwma, 1993). Though their sample would have been crude by today's standards (due to less refined hardware), the methodology used in this first paper is essentially the same as that which is still used. The first step is the deposition of a protective capping layer of carbon or a metal such as tungsten or platinum on top of the region of interest (ROI). This serves to protect the surface from damage from the ion beam, as well as prevent uneven removal of material due to the angle-dependence of sputter yield. If the ROI is near the surface, an initial protective layer can be deposited under the electron beam, with a thicker layer deposited under the ion beam afterward. The next step is to cut trenches on either side of the ROI leaving a lamella roughly 1 µm thick in the middle. The stage is then tilted such that the ion beam can cut away the sides and bottom of the lamella free from the bulk such that it is nearly free. If the FIB is equipped with a micromanipulator, the lamella can then be welded to the tip and transferred to a TEM grid. Once attached to the grid, the sample is thinned using progressively lower current ion beams at slightly offset angles of incidence. This continues until the sample is electron transparent. There are many variants of this technique to prepare samples from almost any material in any orientation (Giannuzzi & Stevie, 1999). Samples can be made as thin as 40 nanometers or less using this method, but high-quality results require considerable time and operator expertise. Nonetheless, FIB preparation of samples is ubiquitous in TEM labs due to the unique site-specificity of the technique, and improved methods continue to be published (Li, Habler, Baldwin, & Abart, 2018).

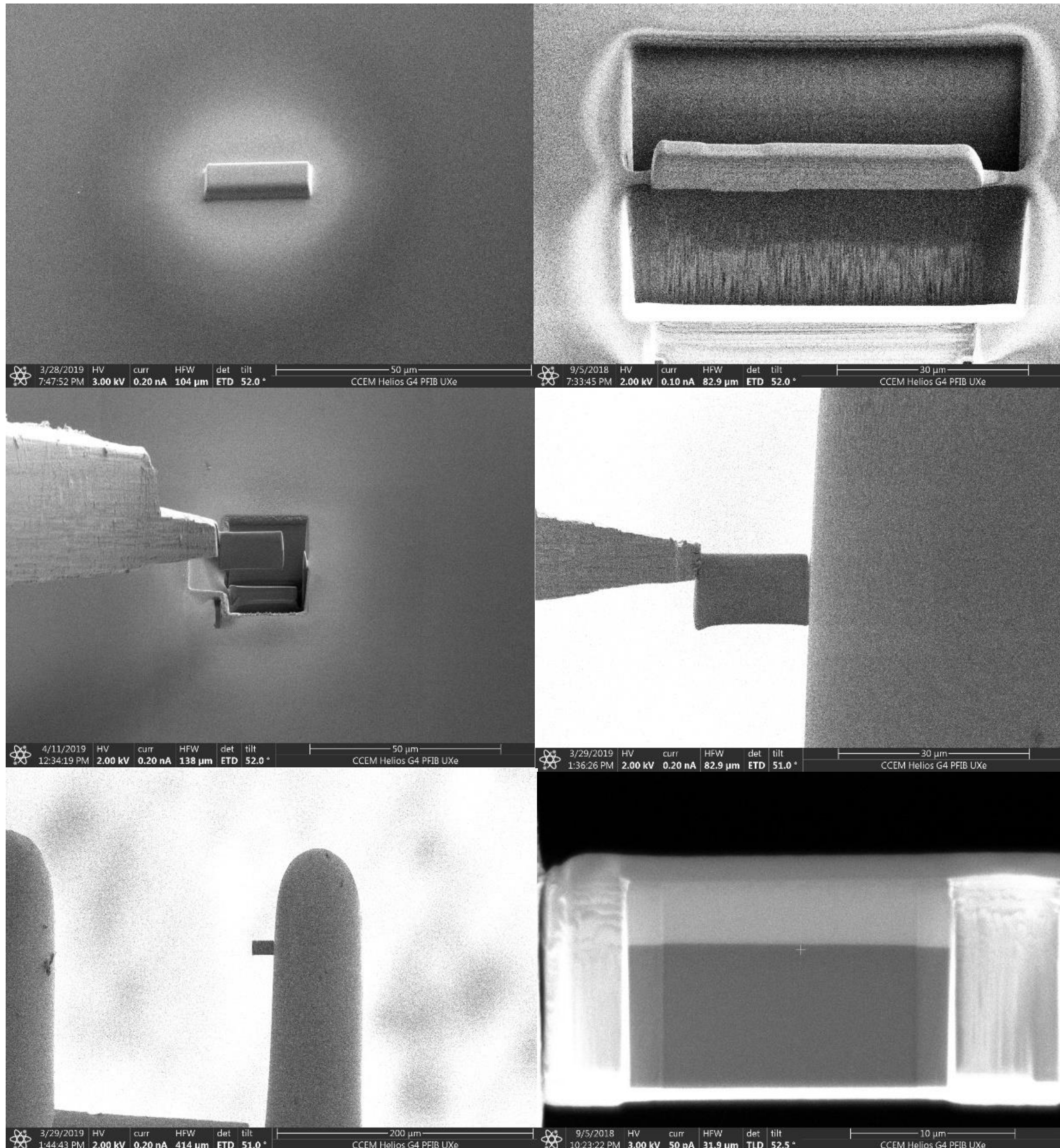


**FIGURE 2.5: STEPS OF THE FIB LIFTOUT PROCESS: A) PROTECTIVE METAL CAP, B) ROUGH TRENCH CUTS, C) MICROMANIPULATOR LIFTING LAMELLA FROM BULK, D) WELDING LAMELLA TO TEM GRID E) THINNING LAMELLA TO ELECTRON TRANSPARENCY**

Five years later, preparation of APT samples was proposed (Larson et al., 1998). Atom probe tips must be very sharp, with a tip radius on the scale of 10 - 100 nm. The most common existing method of sample preparation was chemical electropolishing, but this became complex or impossible with nonconductive samples, and more importantly lacked the site-specificity of FIB. Several different FIB methods were suggested, including a top-down annular milling pattern and a series of angled cuts. Today APT preparation is a common FIB application, and methods continue to be refined, including recent demonstration of xenon PFIB for APT sample preparation (Halpin et al., 2019).

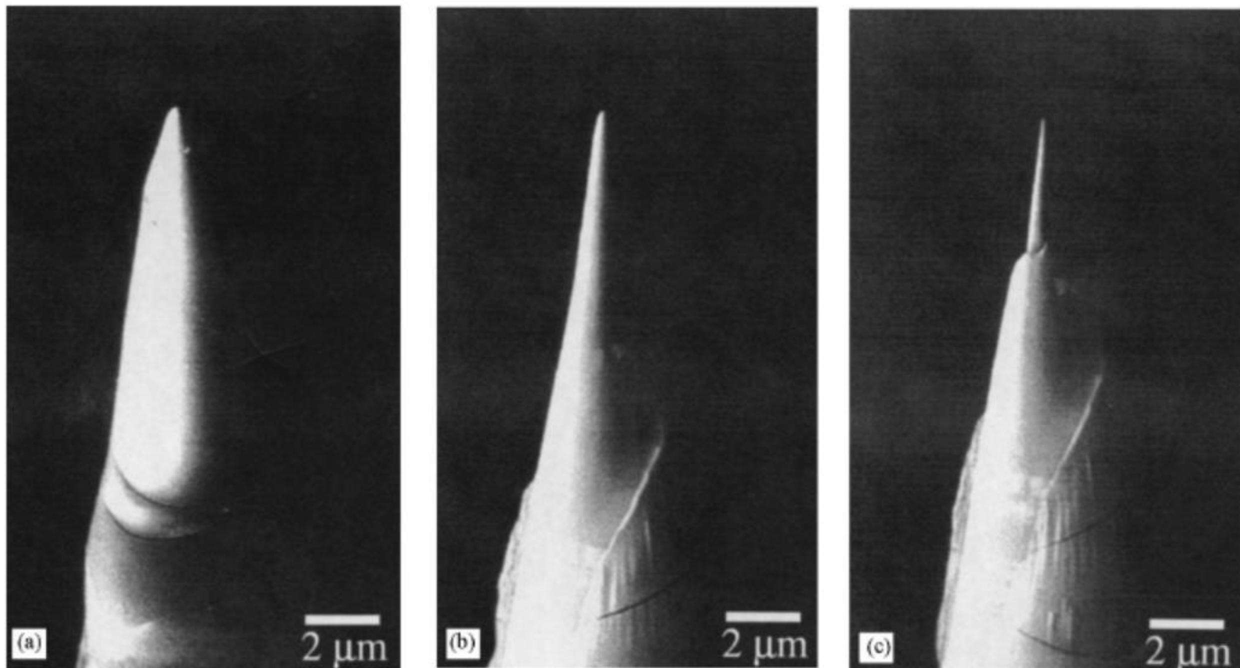


**FIGURE 2.6: STAGES OF ATOM PROBE SAMPLE PREPARATION WITH FIB (FROM LARSON, FOORD ET AL. 1998)**

### 2.2.3 NANOTOMOGRAPHY

A major application developed in the era of single-beam FIBs, but that became widely adopted with advances in dual beam instruments is serial-sectioning nanotomography (Inkson, Mulvihill, & Möbus, 2001). FIB/SEM fills the gap between the existing tomographic techniques of nanometer-scale electron tomography in the TEM and micrometer to millimeter scale x-ray computed tomography (CT). In dual-beam FIB serial sectioning, a sample is oriented with the top surface normal to the ion beam and at an angle (generally 52-55 degrees, depending on microscope manufacturer) to the electron beam (see figure 2.7).

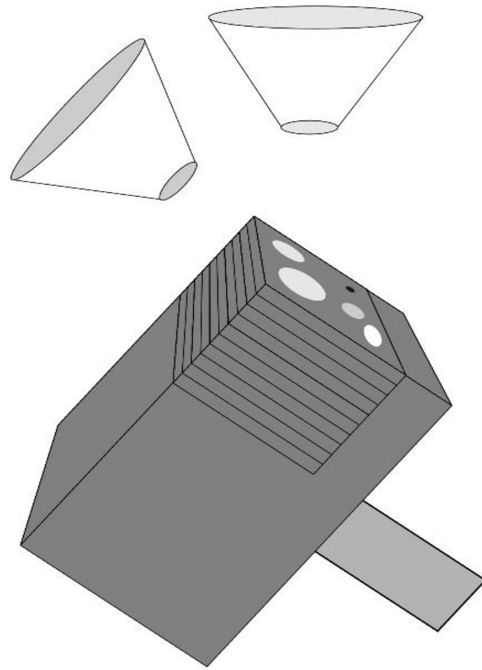

FIGURE 2.7: SCHEMATIC OF TYPICAL FIB TOMOGRAPHY SETUP

A slice of predetermined thickness is milled by the ion beam, followed by an imaging step with the electron beam, which can also include energy-dispersive X-ray spectroscopy (EDS), electron backscatter diffraction (EBSD), or other analytical techniques if desired. This process is repeated until the volume of interest has been analyzed and data can be reconstructed. Acquisition of a high-resolution data set generally requires hundreds of slices over multiple days (particularly for multi-modal imaging), so a highly stable system and automation are required. FIB nanotomography is widely applied in samples with sophisticated porosity or connectivity information, such as multi-phase composites and biological materials. For a brief review of current FIB tomography concepts and techniques, see (Cantoni & Holzer, 2014).

### 2.2.4 PHOTONIC DEVICE FABRICATION

The high resolution and material-independence of FIB techniques makes it a promising tool for direct-write lithography. Standard complementary metal oxide semiconductor (CMOS) fabrication methods require many steps and tools. At its simplest, making a mask for photolithography requires a substrate to be coated with resist, exposed using electron beam lithography (EBL), developed with a solvent, either chemically etched or coated with a layer of metal, then cleaned. FIB eliminates those steps: due to the focus of the beam, no resists, chemical etching, or EBL are necessary; features can be directly written. As described above, FIB has long been used to repair photomasks, but there is still

underdeveloped potential for application in the related field of photonic device microfabrication. Since the advent of fiber optic communication in the 1970s, there has been a push to increase the integration

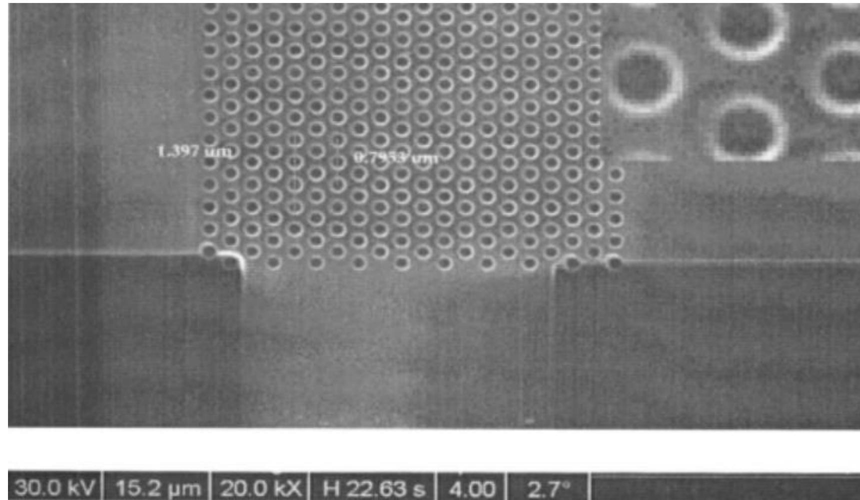


FIGURE 2.8: FIB-FABRICATED PHOTONIC CRYSTAL (FROM BALASAUBRAMANIAN ET AL)

of optical devices in hopes of bringing the benefits enjoyed by long-range optical communication to within the datacenter scale and eventually within individual computers. Many photonic device fabrication techniques were adopted from existing microelectronics manufacturing technology, due to the refined precision of the processes and potential for mass production. However, the silicon-based CMOS methods are not compatible with many of the materials necessary for photonics, such as indium phosphide, gallium arsenide, and other III-V semiconductors.

The first simple application of FIB milling to optical or photonic devices was in published in 1986 (Harriott, Scotti, Cummings, & Ambrose, 1986), with FIB polishing of waveguide facets to reduce optical loss in InP. Since then, other efforts have included 2D photonic crystals (Cryan et al., 2005) and semiconductor lasers (Balasubramanian, Heard, & Cryan, 2006).

## 2.3 ION BEAM DAMAGE

In each application described above, one of the most important considerations when selecting FIB as a processing tool is the sample’s tolerance to damage from the ion beam. Removal of material by sputtering (the process we consider “milling”) is only one of the effects of the primary beam on the surface: other mechanisms can leave residual damage in the sample.

When an energetic ion encounters a solid surface, it may interact with both the sample electrons and the nuclei they surround. The processes of transferring energy are thus termed electronic and nuclear stopping. Electronic stopping is a relatively weak effect: small amounts of energy are

transferred to the sample as phonons and the ion's trajectory is only slightly changed. When an ion undergoes nuclear stopping, however, a large amount of momentum is transferred. The primary ion trajectory changes dramatically, sometimes leading to backscattering. Additionally, the sample nucleus is dislodged from its position in the lattice - a process known as dislocation. Depending on trajectory, the dislocated atom can then escape the sample surface (sputter) and be removed by the vacuum system or penetrate farther into the sample. In the latter case, the sample atom dislocates other atoms until the kinetic energy is expended and it comes to rest in an interstitial position (implantation) (Ivo Utke, 2012). A chain of many secondary collisions and displacements is known as a cascade, which defines the extent of the interaction volume - each incident beam ion may undergo hundreds of additional collisions with sample atoms. At the dose levels used for ion milling, this leads to total amorphization of crystalline samples (and radiolysis of molecular samples) up to the depth of the interaction volume.

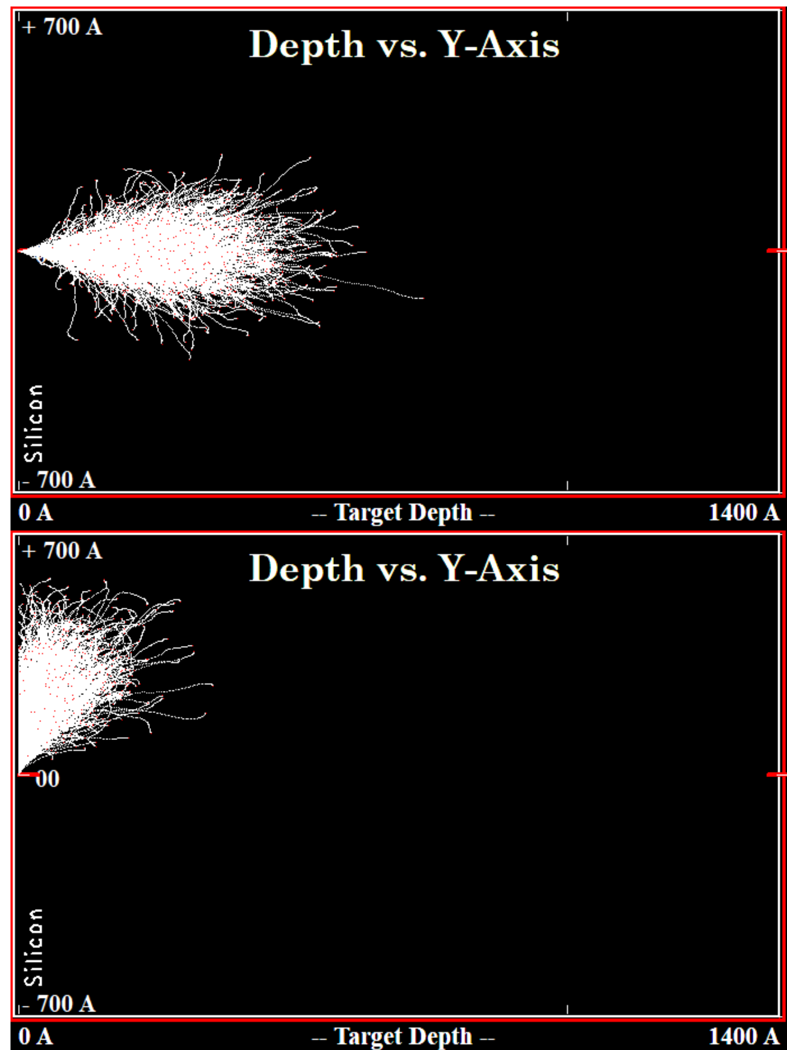


FIGURE 2.9: SIMULATION OF 30 KV ION TRAJECTORIES IN SILICON TOP) NORMAL INCIDENCE, MEAN RANGE OF 27.9 NM. BOTTOM) 88° ANGLE OF INCIDENCE, MEAN RANGE OF 8.0 NM.

A thick FIB-induced amorphous layer is problematic for high-resolution TEM characterization; however, several strategies exist to mitigate FIB damage during TEM preparation. These include milling almost parallel to the surface such that the interaction volume is mostly limited to the lateral straggle of the beam ions (see Figure 2.9). Second, the final surface polishing step is often done at lower ion beam energy, such as 5 or 2 kV, to limit the interaction volume. Finally, a low-energy broad-beam argon ion polishing tool can be used after FIB preparation to further reduce the damaged area (Kato, Kohno, & Saka, 1999).

These techniques can reduce the damaged layer in TEM samples to below 5 nm but are only applicable to the particular geometry seen in TEM sample preparation (milling at the edge, or with a poorly focused low-energy beam). In standard silicon processing, it is possible to “heal” lattice damage

by annealing the wafers. However, in other material systems common in photonic device fabrication (such as indium phosphide), annealing is not possible without destroying the device. Other methods of removing the damaged layer include broad beam low-energy ion milling and chemical etching, but these methods are not site specific and are material-dependent. The best way to eliminate the detrimental effects of ion beam-induced surface damage is to reduce the degree of damage in the first place.

## 2.4 CHARACTERIZATION TECHNIQUES

In order to compare the gallium and xenon ion sources, thorough characterization of beam damage was needed. To evaluate ion beam damage, TEM/EELS and Raman spectroscopy were used. These techniques were used because this experiment required 1) chemical information at spatial resolution only attainable in the TEM and 2) information about optical properties at lower spatial resolution.

### 2.4.1 Transmission electron microscopy/electron energy loss spectroscopy

The first electron microscope to surpass the Abbe resolution limit was built by Ernst Ruska in 1933, for which he won the Nobel prize in 1986. His microscope operated by accelerating a focused beam of electrons through a thin sample and capturing the scattered electrons below the sample with a phosphor plate (scintillator). This initial design was developed extensively through the 20$^{th}$ century into the modern TEM. While this technique does not have resolving power in the Z dimension (which an SEM does have), it provides a wealth of information about the sample. The two primary modes of operation in a TEM are imaging and diffraction. In imaging mode, electrons are demagnified and collimated into a parallel beam by a series of condenser lenses, scattered through the sample and a series of projector lenses, and recorded by a detector. Scattering probability (known as cross-section) is dependent on atomic number and sample thickness: this provides chemical contrast at high spatial resolution, especially when the beam is focused and rastered across the sample which is known as scanning-transmission mode (STEM). By inserting an aperture into the back focal plane of the objective lens, crystallographic information may also be collected. Instead of an image with spatial information, a diffraction pattern is acquired. The diffraction pattern is the Fourier transform of the electron wave's interaction with the crystal lattice. By measuring the spacing and orientation of spots in the diffraction pattern, the atomic positions and lattice parameters of a unit cell can be determined. Diffraction and imaging are the most fundamental techniques applied in the TEM, but there are myriad other methods, both with the scintillator detector and other types of detector. These include EDS detectors, backscattered electron detectors, high-angle annular darkfield detectors (HAADF), and more. For an extensive introduction to TEM and its many modalities, see the

comprehensive text by Williams and Carter. One of the most popular TEM techniques continuing to develop in the 21st century is electron energy loss spectroscopy (EELS).

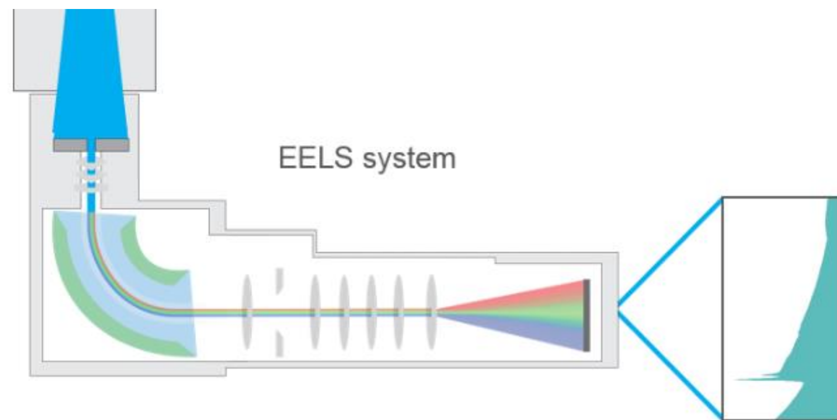


FIGURE 2.10: SCHEMATIC OF EELS INSTRUMENTATION (COURTESY GATAN)

While the concept of measuring energy transfer from primary electrons to a sample within a TEM has been around since the 1940s (Hillier & Baker, 1944), instrumentation precise enough to utilize the theory has only been commercially produced since the 1990s. Today, EELS is a popular and versatile technique for the measurement of composition, bonding, valence state, and electronic properties of most materials. As primary beam electrons pass through a sample, a fraction of them undergo inelastic scattering events. By measuring the difference in energy from that of the primary beam (the zero-loss peak [ZLP]), the scattering event that led to the energy loss can be reconstructed. EELS spectroscopy requires a TEM equipped with a magnetic prism (after the sample and projector lenses) to disperse electrons by energy along one axis, followed by a series of apertures to reject all but a specific range of energies. Additionally, STEM mode is almost always used for EELS, as it enables collection of a spectrum from each individual pixel as the beam rasters across the sample, creating a map of composition. Since electrons can undergo multiple scattering events, samples must be thin and of high quality; the greater number of scattering events that take place in thicker samples causes peak broadening. For example, the major peak visible in the silicon EELS spectrum is at 1839 eV, which corresponds to the onset of the silicon K-shell absorption edge.

### 2.4.2 RAMAN SPECTROSCOPY

The Raman effect was first discovered in the late 1920's by K.S. Krishnan and C.V. Raman (who won the 1930 Nobel prize in physics for his efforts). When light passes through a medium, a small fraction is scattered (absorbed and instantly re-emitted). Most of this light is scattered at the same

wavelength as the incident light, but about 0.1% is shifted to either lower or higher energy (Stokes and anti-Stokes shifts, respectively).

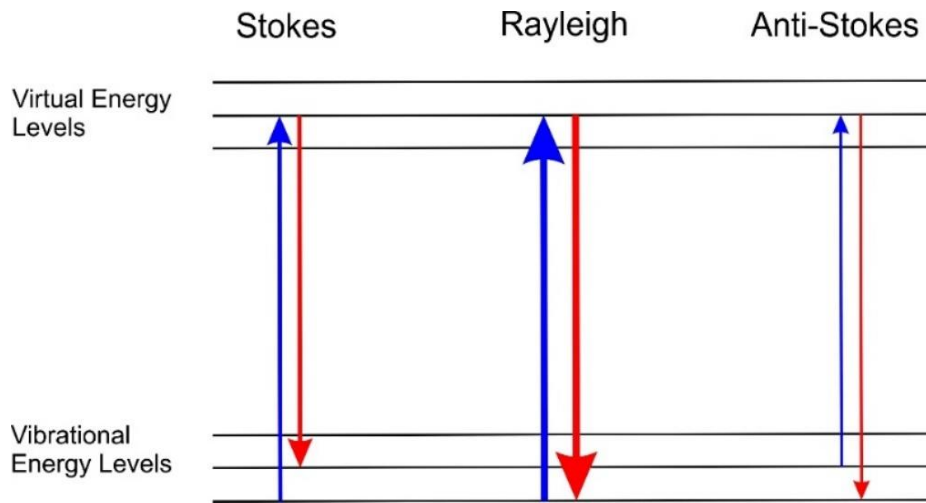


FIGURE 2.11: RAYLEIGH VS. RAMAN SCATTERING

The extent of the shift is dependent on the energy of the bonds in the scattering medium (in crystalline samples, the phonon modes in the lattice); hence the Raman effect was quickly developed into a spectroscopic tool for chemical characterization. In the 1960s, development of the high-intensity laser sources needed to excite the Raman effect to a measurable degree made Raman spectroscopy much easier in practice, and soon it became a standard characterization technique for diverse liquid, solid, and gas phase samples.

The spectra for single-crystal samples is generally rather simple – in the case of silicon, a single strong peak is apparent at a shift of 520 $cm^{-1}$ for the triply degenerate first-order transverse optical (TO) phonon mode in silicon (the second-order TO and second-order transverse acoustic (TA) peaks are sometimes visible as well, but at least two orders of magnitude weaker). The intensity of the peak depends on the efficiency with which the Raman excitation laser can couple to phonons in the lattice.

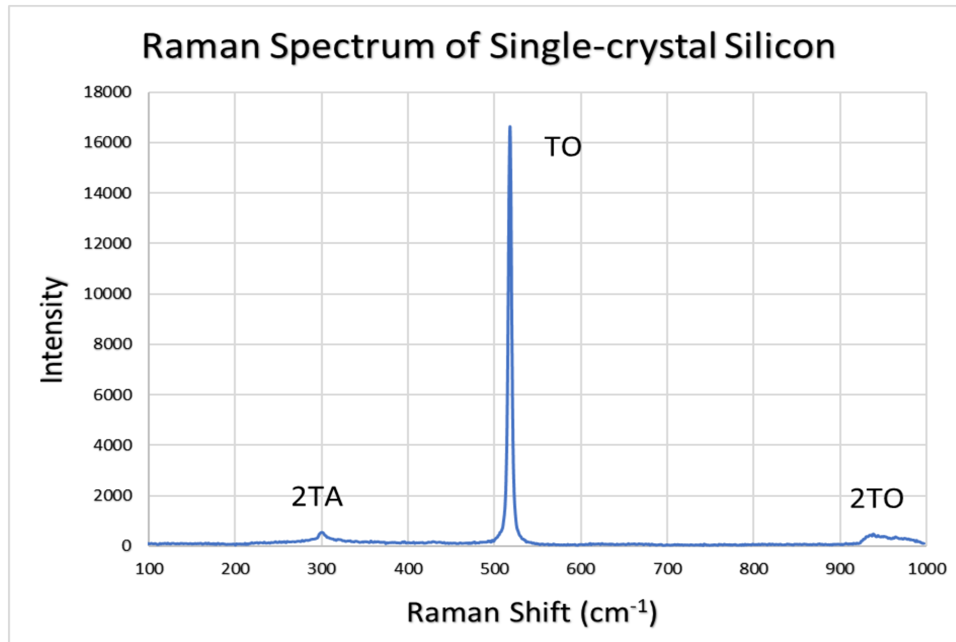


FIGURE 2.12: RAMAN SPECTRUM OF SINGLE-CRYSTAL SILICON

Modern Raman systems genenrally offer a choice of excitations lasers that may be selected to couple most strongly with the sample under analysis.

Amorphous silicon has a broad peak centered at 480 $cm^{-1}$ due to the many different bonding configurations and atomic spacings possible.

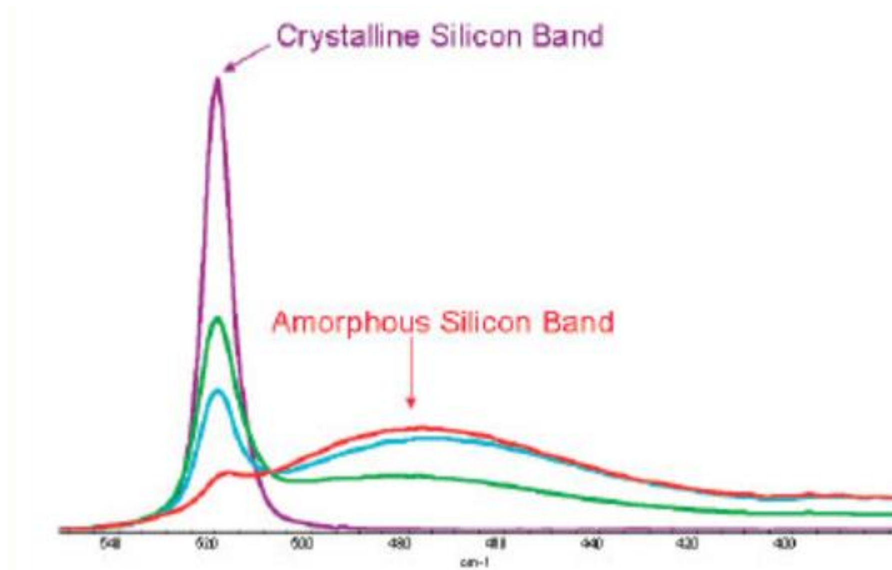


FIGURE 2.13: RAMAN SPECTRUM OF SINGLE-CRYSTAL AND AMORPHOUS SILICON (COURTESY THERMOFISHER)

# CHAPTER 3: EXPERIMENTS AND METHODS

## 3.1 PHOTONIC DEVICE FABRICATION

Chronologically, the first research carried out was the fabrication of several types of micro-optical devices. For reasons described above, FIB has long had great potential to be adopted as a prototyping tool in this field. In the following section, the process of fabricating some devices with both the gallium and xenon FIB will be described, including principles of device operation and any optical measurements carried out on prototype devices.

### 3.1.1 WAVEGUIDE END FACETS

A critical factor in the design of integrated optical circuits is the level of acceptable power losses as light is transmitted through the circuit, since boosting the signal on-chip requires additional amplifiers or laser sources, adding considerable complexity. Therefore, it is important to minimize the loss from coupling (bringing light onto the optical chip from an off-chip fiber optic cable). Generally, when integrated photonic circuits are fabricated on a wafer following traditional semiconductor fabrication techniques, the wafer must be diced with a saw or laser to separate individual chips from the whole wafer. This process is problematic, since the rough surface finish of diced chip edges causes significant scattering loss during coupling into waveguides or other on-chip devices. The issue is particularly evident in systems with multiple materials with different thermal or mechanical properties, such as silicon-on-insulator (SOI). The oxide layer on an SOI chip is much less thermally conductive than the bulk silicon (1.3 compared to 149 $Wm^{-1}K$) and hence is pulled and distorted during the dicing process, as seen in Figure 3.1 (Glassbrenner & Slack, 1964). The significant optical losses from the rough facets create difficulty when attempting to test waveguide designs; enough light must couple into the waveguide, propagate through considerable distance and around any deliberately designed bends and devices, and reach a detector with enough power to give reliable measurements. Minimizing loss from chip edges allows more precise measurement of losses on the chip itself.

To evaluate the value of FIB for modifying waveguide facets, a gallium-source NVision 40 (Zeiss GmbH, Germany) FIB was used to polish waveguide edges to mirror quality to minimize coupling loss. A series of straight and “paperclip” curved silicon nitride (SiN) waveguides ranging from 1 to 2 µm in width were selected for this experiment. First, loss from the as-delivered waveguides was measured by coupling a 1550 nm wavelength source through a single-mode fiber (SMF) through a waveguide (onto and off of the chip) and into a power meter. Both facets of each of the selected waveguides were then

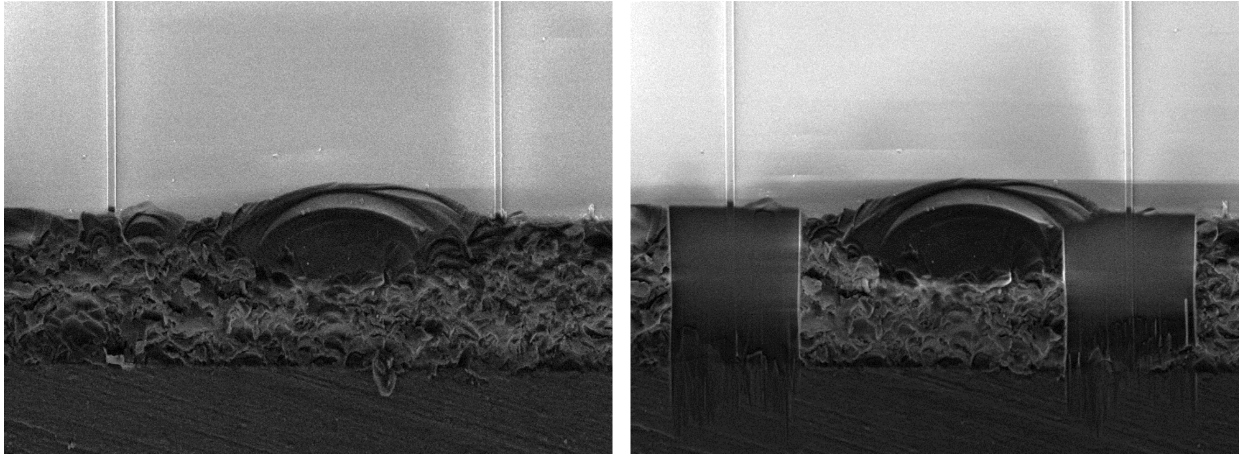

FIGURE 3.1: LEFT) EDGE FACET OF AN SOI CHIP AS DICED. RIGHT) FIB-PROCESSED WAVEGUIDE FACETS

TABLE 3.1: LOSS MEASUREMENTS BEFORE AND AFTER FIB-FACETING

| Width | R4, 2.2cm, before FIB | R4, 2.2cm, after FIB |
|---|---|---|
| 1.4 µ | -19.7db | -13.5db |
| 1.6 µ | -18db | -13.5db |
| 1.8 µ | -15.2db | -12db |
| 2.0 µ | -27.8db | -15.1db |

milled for 90 seconds at normal incidence. A low beam current of 40 pA was chosen to maintain sharp edges on the chip and reduce curtaining artifacts introduced by the edges of the waveguides (see Figure 3.1). The lateral size of the facet was chosen to match roughly the area of the optical mode within the chip, and the depth of the facet was chosen to ensure that all roughness (or chipped waveguide ends) was eliminated. After FIB milling, the loss was measured again to determine effectiveness.

FIB-milled facets were shown to reduce coupling loss by a factor of 5 on average (see Table 3.1). This process was not optimized for time; with automation this technique shows high value for modifying

or repairing unique high-loss devices, especially in a university setting. This also allows a consistent method to reduce coupling loss in order to measure the true optical properties of the waveguide as-designed.

### 3.1.2 DFB Laser

A current limitation in silicon photonics is a lack of on-chip laser sources that are cheap, efficient, tunable, and small (Zhou, Yin, & Michel, 2015). A type of laser that may fill all of these needs is the distributed feedback (DFB) laser. In this work, an indium phosphide optical amplifier (pictured in Figure 3.2) was used as a starting substrate (though a silicon-based device could have also been used). To convert from a broadband optical amplifier to a single mode laser, two FIB modifications were needed. First, a cavity needed to be created: to do this, mirror facets were milled at each side of the

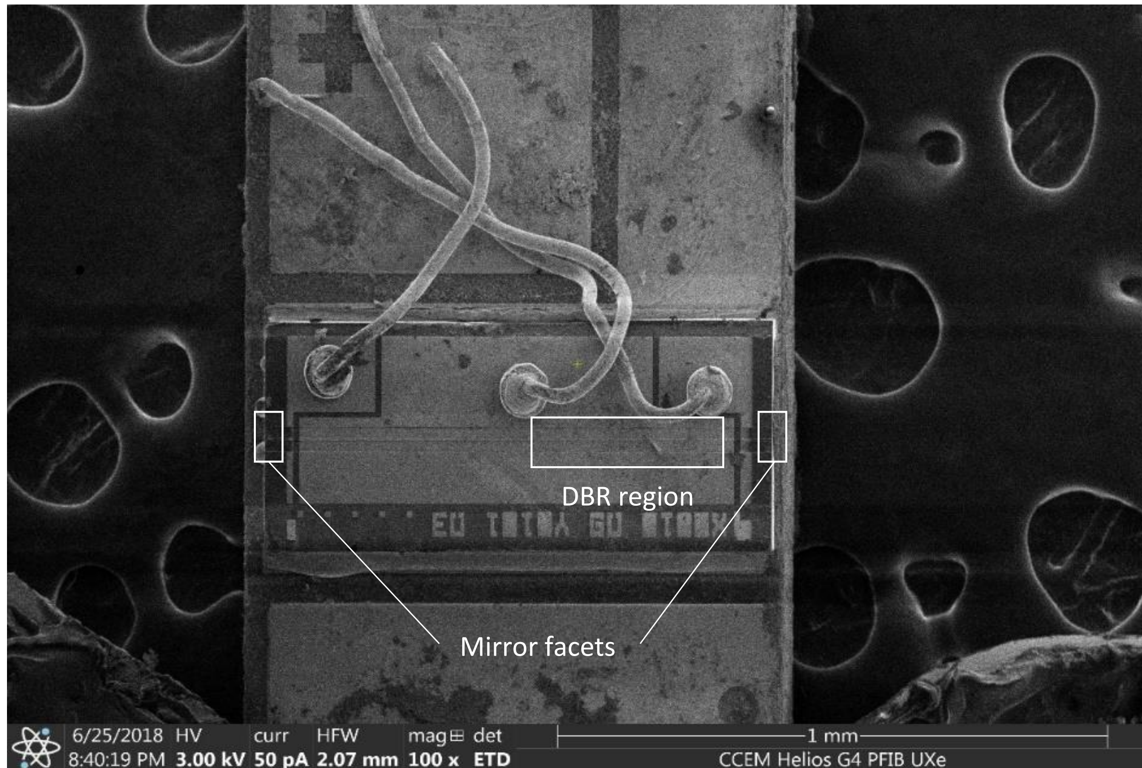


FIGURE 3.2: SEM MICROGRAPH OF AN INDIUM PHOSPHIDE OPTICAL AMPLIFIER BEFORE FIB MODIFICATION

chip. Second, a single wavelength (1550 nm in this case) needed to be selected. To do this, a distributed Bragg reflector (DBR) was milled into a portion of the amplifier waveguide. The principle of operation for the DBR is that for a specific grating pitch there is only one wavelength that fulfills the Bragg condition and is therefore reflected. All other wavelengths are transmitted. In this way, the reflected wavelength is confined in cavity and can build up to a threshold optical power and begin to lase, while other

wavelengths are transmitted either to other components or to a power sink (see schematic in Figure 3.3).

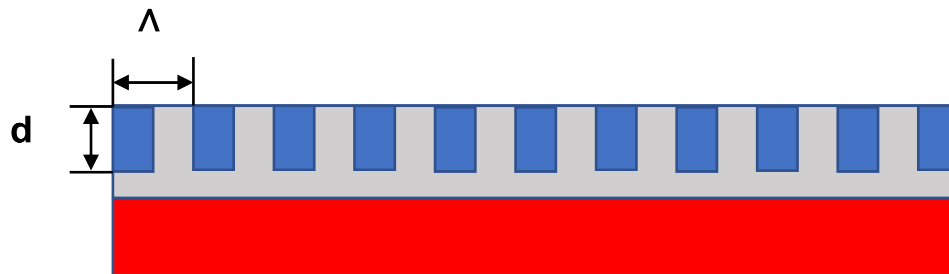


FIGURE 3.3: SCHEMATIC OF DISTRIBUTED BRAGG REFLECTOR

$$\Lambda = \frac{\lambda}{2 * n}$$

Where Λ is grating period, λ is operating wavelength, and *n* is index of refraction. To satisfy the

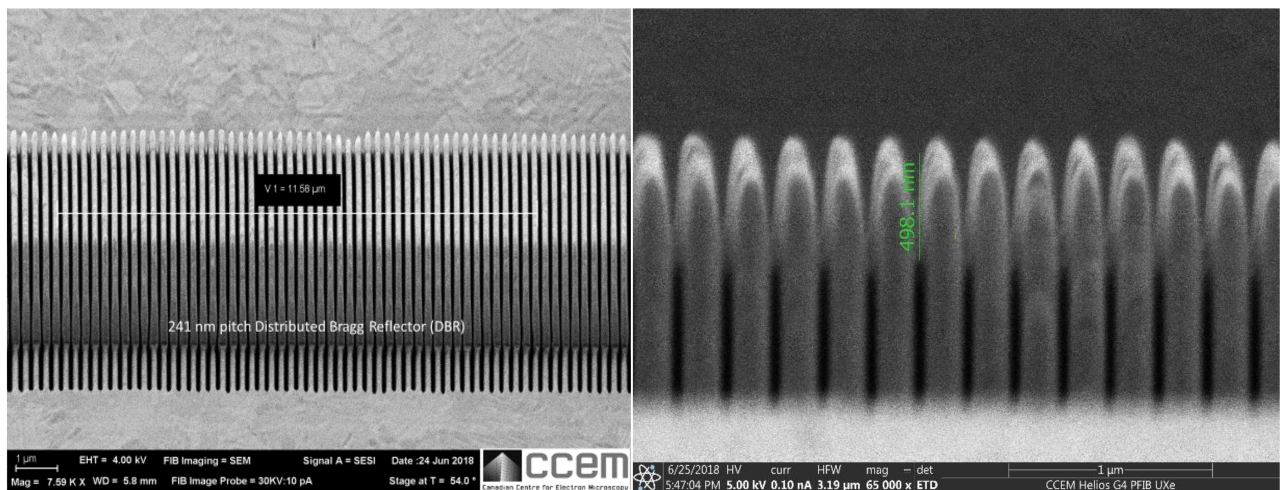


FIGURE 3.4: LEFT) DISTRIBUTED BRAGG REFLECTOR RIGHT) DETAIL OF 241 NM PITCH

Bragg condition for a laser operating at 1550 nm, the period was chosen to be 241 nm. Using the Nanopatterning and Visualization Engine software (Fibics Inc., Canada) to guide the scanning path of the NVision FIB, a grating 150 µm long with 241 nm period was milled into the waveguide with a beam of 30 kV and 30 pA.

SEM measurement showed the experimental pitch to be within ±2 nm of the set value, and consistent across the length of the grating. FIB-modified devices were tested by running various pump currents through the active region and measuring the optical power emitted from the end facet. As seen in Figure 3.5, lasing was achieved with a threshold between 50 and 100 mA of pump current, with the center wavelength shifting to longer wavelengths at higher currents due to heating effects. The

envelope of emission was extremely wide compared to commercially available DFB lasers, which can achieve a linewidth of 0.1 nm at -20 dB. Additionally, the power efficiency was low: an output of roughly 10 µW of optical power at 100 mA of pump current (see figure 3.5), compared to 2 mW of optical power with 20 mA pump available commercially (Thorlabs, 2015). The likely causes of poor performance are FIB-induced damage and pattern drift during fabrication.

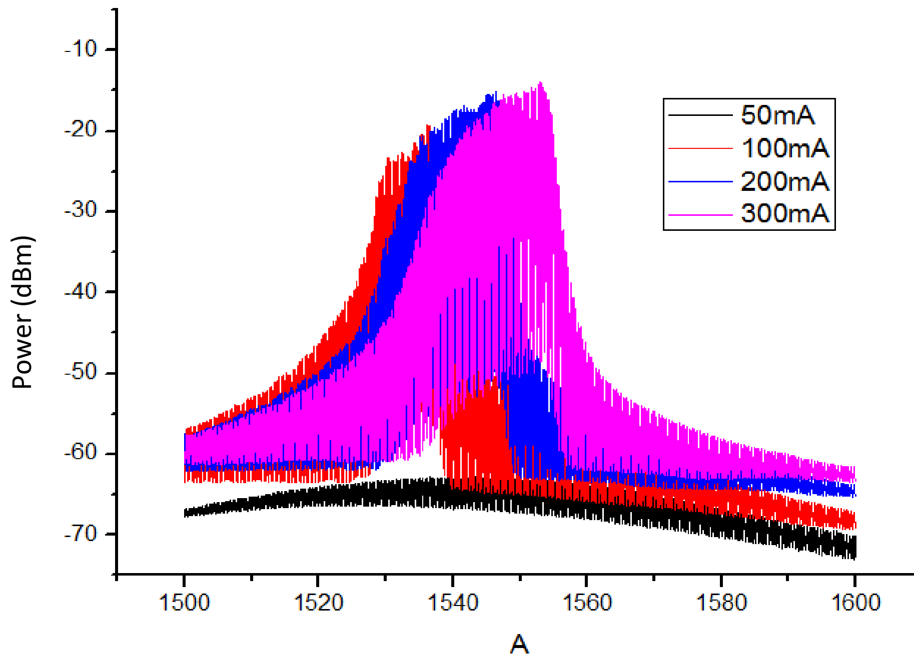


FIGURE 3.5: OPTICAL POWER OUTPUT OF DFB LASER

### 3.1.3 IR POLARIZER

One of the most popular topics in optics since the early 2000s is electromagnetic metamaterials (D. R. Smith, Pendry, & Wiltshire, 2004). A metamaterial is a device or surface that exhibits optical properties not generally found in nature; for instance, with real and imaginary parts of the dielectric function of opposite signs. These phenomena can lead to unusual optical properties such as a negative index of refraction, allowing devices such as perfect lenses and electromagnetic cloaks (Pendry, 2000). One application of optical metamaterials is the development of deeply subwavelength optics, of particular importance in the infrared spectrum (since conventional optics require a larger footprint to accommodate longer wavelengths). Van der Waals crystals have experienced particular attention as a suitable substrate material for metamaterial devices due to the strong anisotropy of their bonding structure.

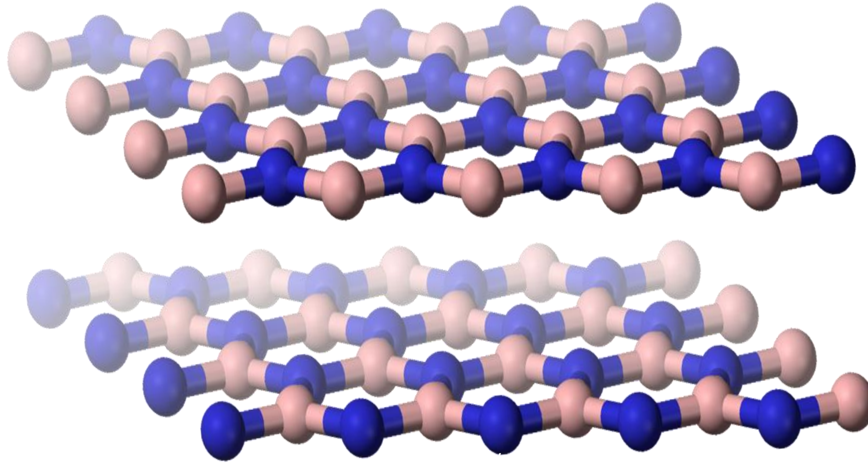

FIGURE 3.6: LATTICE STRUCTURE OF HBN, A VAN DER WAALS CRYSTAL. REPRINTED FROM WIKIPEDIA UNDER CREATIVE COMMONS LICENSE

This enables the well-known procedure of exfoliation as a means to produce uniformly thin flakes of material, as van der Waals crystals exfoliate easily along only one axis (in the case of hBN, the c-axis). Additionally, this anisotropy determines the energies of supported phonon modes (Basov, Fogler, & García de Abajo, 2016). Due to its unique phonon dispersion in the mid-IR range, the van der Waals crystal hexagonal boron nitride (hBN) is known as a hyperbolic material. Mid-IR light can couple into hBN via phonon polaritons, and due to the anisotropic dispersion, energy is confined to propagate in the Z direction (Caldwell et al., 2014). By creating a structure in hBN with multiple depth steps, multiple phase shifts are induced in the electromagnetic wave. When the energy decouples back into free space on the other side of the hBN flake, the series of phase offsets superimpose into a circularly polarized wave.

Arrays of a “staircase” primitive structure were fabricated in a gallium NVision 40 GaFIB (Zeiss GmbH, Germany) with a beam of 30 kV and 30 pA (see Figure 3.7). The substrate was hBN flakes of thickness varying from 100 - 600 nm exfoliated onto an intrinsic silicon wafer. Due to the difference in flake thickness, the exact dose varied for each array: the deepest step was milled entirely through the hBN, with the other two steps at equal distances between the bottom and top of the flake. Array dimensions were 50 x 50 µm. Several array pitches ranging from 1 to 2.5 µm were attempted. Optical characteristics of the devices were measured in transmission using a mid-IR light source at Vanderbilt University. While some resonance was observed demonstrating coupling of the light into the nanostructure array, the desired polarization effect was not seen. Due to the necessity of an intact

lattice near the surface for phonon polariton coupling, it is likely that damage from the ion beam is responsible for the failure of the device. Indeed, milled features possessed small (few nm) beads of gallium distributed across the surface (see inset, figure 3.7). This conclusion led to the next phase of experimentation, directed towards understanding damage characteristics of gallium and xenon beams.

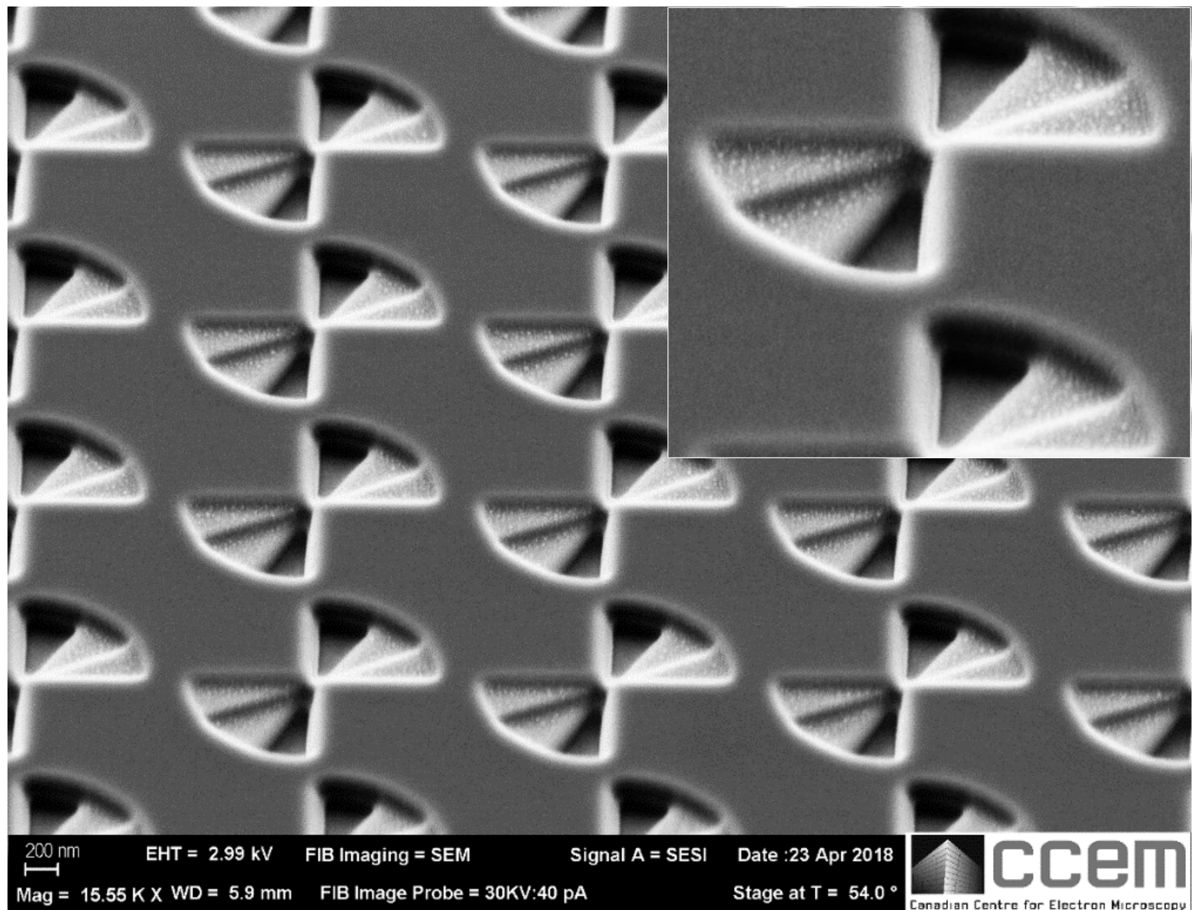


FIGURE 3.7: SEM MICROGRAPH OF IR POLARIZER DEVICE IN HBN. INSET) GALLIUM BEADING ON THE HBN SURFACE.

## 3.2 BEAM DAMAGE

While the devices fabricated in the gallium FIB generally matched the design specifications in physical dimensions, devices often failed to actually function when tested on an optical bench. As demonstrated in earlier work, ion beam damage is likely the cause of this. In some cases, it is possible to repair the damage by using an annealing step to allow the lattice to relax (Chyr, Lee et al. 1999), but this is incompatible with many material systems: for instance, those with low melting-point metal coatings. In order to evaluate whether the PFIB would offer an improvement for device prototyping in terms of beam damage, a side-by-side experiment was carried out with two FIBs – one with a gallium LMIS and one with xenon ICP. The first beam energy selected was 30 kV for both ion sources: this is the most

commonly used beam energy for lithographic applications since it provides the highest sputter yield and resolution available on commercial instruments. The second beam energy was 5 kV on the PFIB and 10 kV on the gallium FIB (10 kV was the lowest energy available on the gallium FIB, while the PFIB was not aligned at 10kV). While most FIB milling occurs at 30 kV, there are some applications (such as TEM sample prep) that utilize a lower kV polishing step due to the smaller interaction volume, so the lower-energy beam damage was also evaluated in the experiments below.

### 3.2.1 TEM/EELS

Samples for TEM were irradiated with both beams at 30 and 10 kV on the gallium FIB, and 30 and 5 kV on the PFIB as described above. For each ion species and beam energy, a low and high dose sample was made. The low dose samples received a dose of 0.0625 nC/μm$^2$, with the high dose samples receiving a dose an order of magnitude greater (0.625 nC/μm$^2$). Additionally, samples were prepared such that an undosed area was part of the region of interest. Since there is no way to prepare TEM samples of FIB-damaged material without additional FIB processing, the preparation method was kept as consistent as possible. All TEM samples were made in the PFIB, so that any preparation-induced artifacts would be equally present in both sets of samples. Special care was taken to ensure that damage from the sample preparation process was not confused with the damage from the intended applied

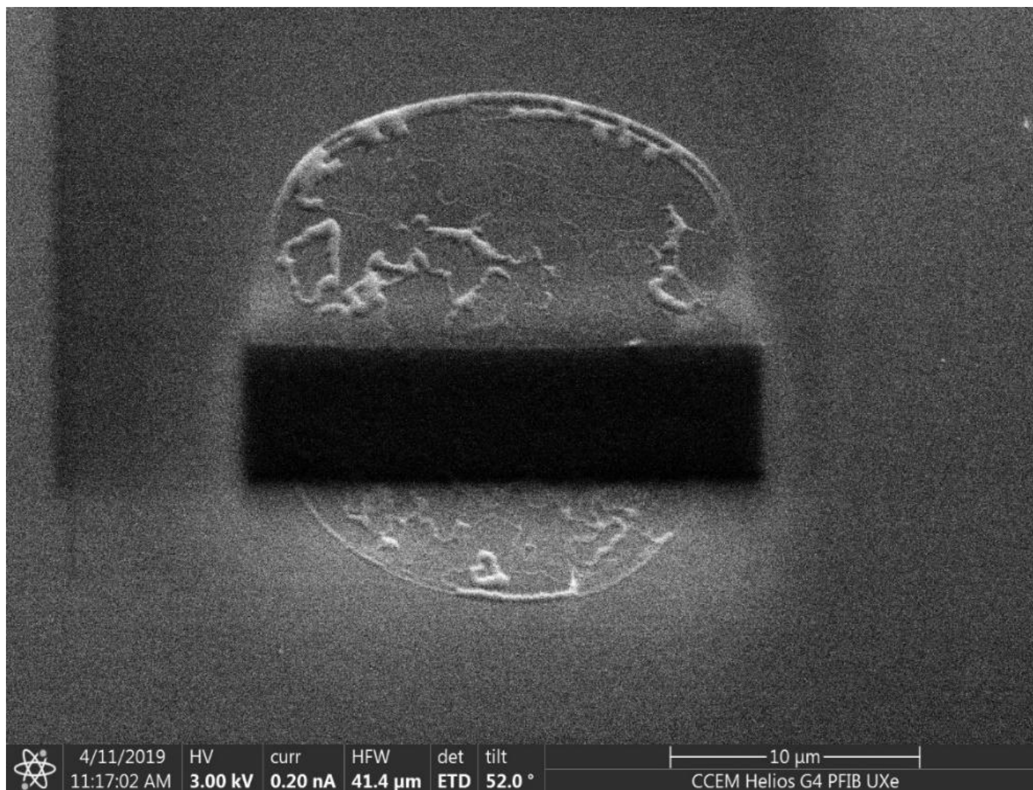


**FIGURE 3.8: E-BEAM DEPOSITED CARBON ON 10 KV GA-IRRADIATED SURFACE**

dose. To prevent this, a layer (approximately 100 nm) of amorphous carbon was deposited on the dosed area using the electron beam before the ion beam was unblanked (see Figure 3.8).

Once the ROI was coated with electron beam carbon, the ion beam was used to rapidly deposit 3 - 5 µm of platinum. Trenches were then cut, the sample extracted with the micromanipulator, attached to a TEM grid, and thinned according to standard *in-situ* liftout procedures (described in section 2.2.2). Lamella thicknesses varied slightly but were all less than 100 nm and therefore suitable for high resolution analysis.

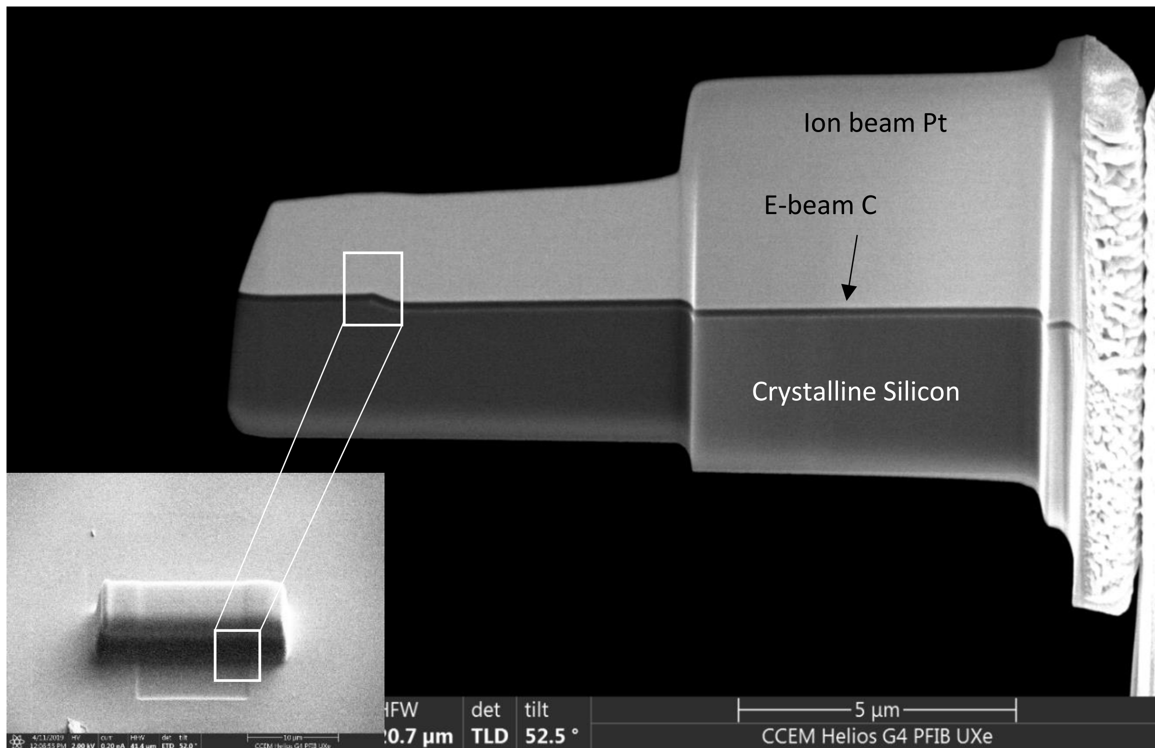


FIGURE 3.9: (INSET) 30 KV GA-IRRADIATED SURFACE AND RESULTING TEM SAMPLE

TEM analysis was carried out in an FEI Titan 80-300 HB (FEI Company, USA). Annular darkfield (ADF) imaging at 200 kV and 150 pA was used to collect high-resolution images of the irradiated surfaces in cross-section at magnification up to 1,000,000x. Images were measured using Digital Micrograph (Gatan, USA) to determine the thickness of the amorphized layer under each ion beam condition. They were also used to qualitatively analyze nanostructural features within each sample surface, such as gallium clustering or dopant segregation. While only single samples were made of each beam setting, the amorphous layer thickness was constant within a few nanometers across the entire samples (5 – 8 µm). In addition, the experimentally measured thickness was very close to the maximum penetration depth observed in simulation.

Following high resolution imaging, EELS spectroscopy was performed. The K2 direct electron detector was used for its high sensitivity, and TEM beam current was increased to 300 pA to improve the signal to noise ratio (Chiu et al., 2015). EELS maps were acquired in STEM mode in order to visualize where dopant species were implanted, and peak height ratio comparison was used as an estimate of relative concentration.

### 3.2.3 Raman Spectroscopy

While TEM/EELS provides a wealth of information about atomic-resolution lattice structure and chemical composition, it is a time and cost-intensive technique. For a faster and simpler method of diagnosing the severity of ion beam damage, Raman spectroscopy was used. Arrays of 12 µm x 12 µm

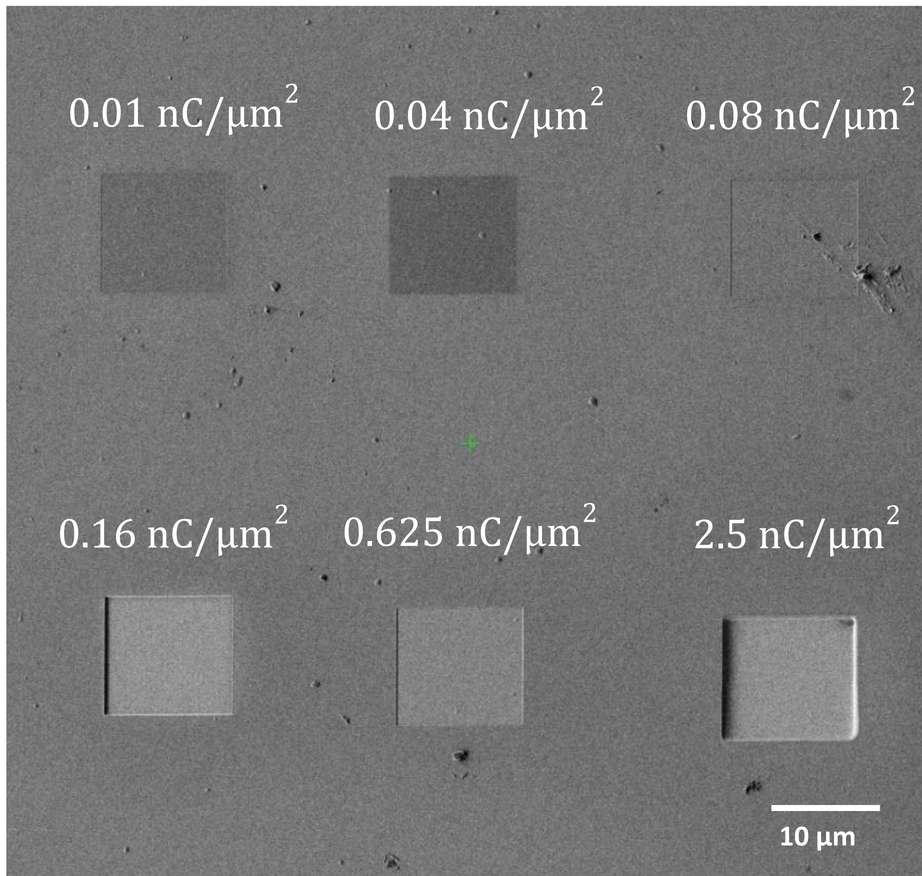


**Figure 3.10: Example of dose array for damage characterization by Raman**

squares were irradiated (see Figure 3.10) in each FIB at a range of several ion doses and two beam energies. The doses were distributed from 0 up to a “saturation” level: when a depth greater than the ion interaction volume had been milled and it was assumed that maximum damage had occurred.

A Renishaw InVia Reflex Raman microscope (Renishaw PLC, UK) was used for this experiment. Three excitation lasers were available: 514 nm, 633 nm, and 785 nm. Test data was acquired with each laser to evaluate the best one for this experiment. The spectra were nearly identical, so the 514 nm laser was chosen for its shallower penetration depth and higher signal to noise ratio. 1% laser power was used, and the spectrometer was scanned from 200 to 800 $cm^{-1}$ (centered on the primary Si Raman peak of 520 $cm^{-1}$). Each scan was 30 seconds long, and 5 scans were averaged in each acquisition. Five reference spectra of unexposed silicon were acquired at various distances from the exposed areas to ensure that the Raman intensity from undamaged silicon was consistent and not effected by beam tails.

# CHAPTER 4: RESULTS AND DISCUSSION

Previous publications have shown that gallium beam damage can be a crucial consideration when using FIB as a tool for photonic device prototyping (DeFreez, 1991; Harriott, Scotti, et al., 1986). Nearly all of the works that demonstrate a functioning optical device utilized a post-processing step to mitigate the effects of beam damage, usually a chemical etching step. Unfortunately, the use of a chemical etchant eliminates one of the main advantages of However, these studies have not included a detailed analysis of the damage itself. Most beam damage research has been carried out with the goal of improving TEM sample preparation procedures, hence these studies disregard effects on optical properties, and the only characterization technique necessary was TEM itself (Kato et al., 1999; McCaffrey, Phaneuf, & Madsen, 2001). In the past year, some papers have demonstrated the viability of Raman spectroscopy as a method of evaluating optical damage from the gallium FIB (Aydin, Carl, Philip, James, & Haider, 2015; Deshpande, Vilayurganapathy, Bhat, & Ghosh, 2019). There is very little research published regarding xenon beam damage. To understand beam damage from both gallium and xenon FIBs and effects on FIB-milled optical devices, an experiment was performed utilizing both TEM/EELS and Raman spectroscopy to characterize silicon exposed to the ion beams.

The first step to understanding what happens to ions when they hit a surface was to carry out SRIM simulations (Ziegler, 2008). SRIM is a Monte Carlo based software package that models the collisions of ions of a certain species and energy with a substrate. While SRIM utilizes the binary collision approximation (BCA) and does not account for sample crystallinity, the empirical stopping constants for silicon have been very finely tweaked over many experiments and are very accurate. Even at first glance, there are obvious differences in the interaction volume of xenon and gallium ions (Figure 4.1). Due to its larger van der Waals radius (216 pm vs. 187 pm for gallium), xenon is less likely to channel between atomic columns and more likely to undergo a nuclear stopping event near the sample surface, leading to a smaller interaction volume (Bondi, 1964).

The next step was to evaluate the accuracy of the SRIM interaction volumes using high resolution STEM. STEM imaging with EELS spectroscopy is the gold standard for characterizing structure and composition of nanometer-scale features. It is the only technique capable of providing a precise measurement of thickness of the amorphous layer, while simultaneously mapping the distribution of elemental impurities. Image measurements confirmed that the SRIM software accurately calculated the maximum penetration depth of the ions into silicon.

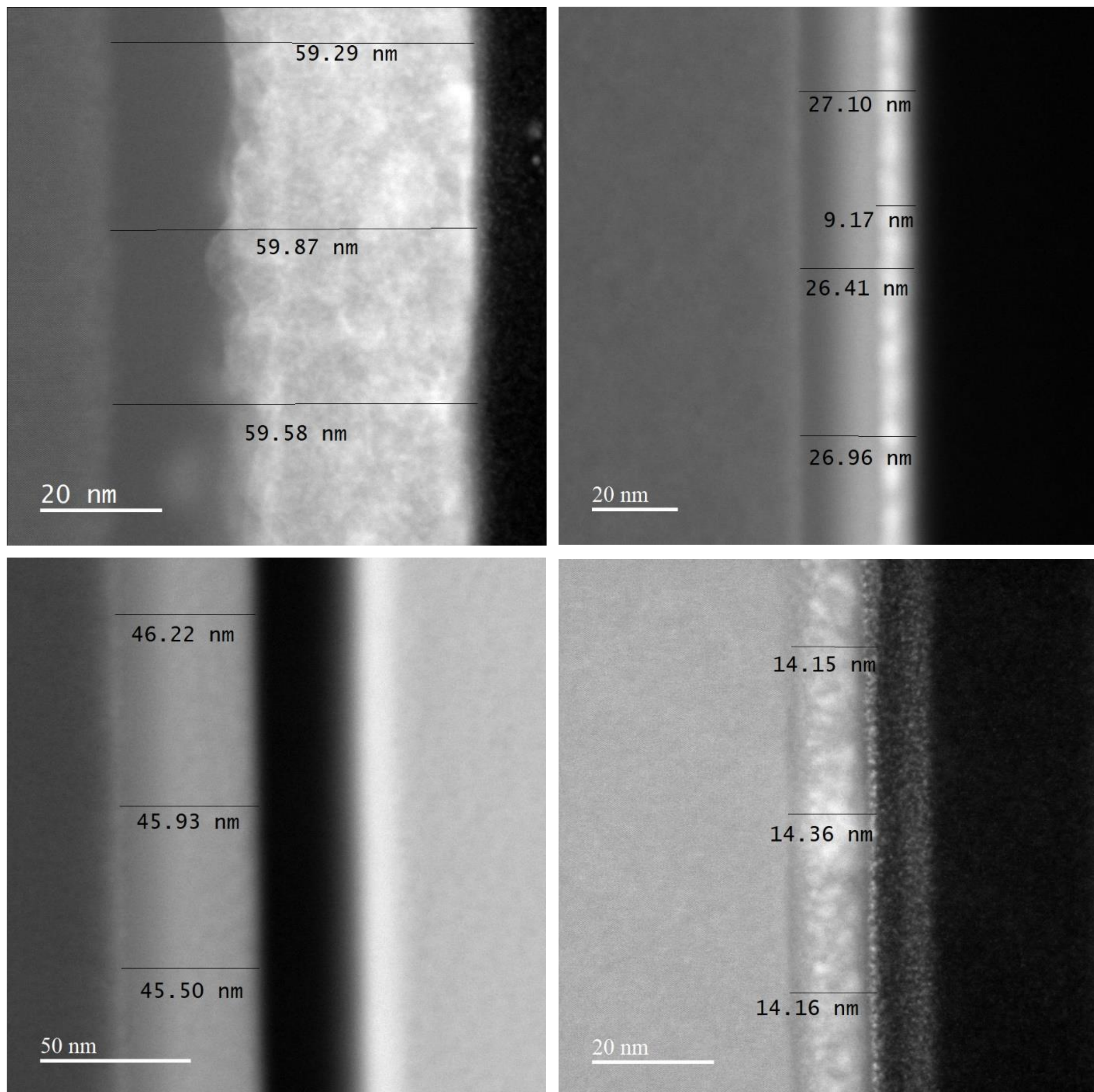


FIGURE 4.1: ADF IMAGES OF HIGH-DOSE ION BEAM DAMAGE. TOP LEFT) 30 KV GALLIUM, TOP RIGHT) 10 KV GALLIUM, BOTTOM LEFT) 30KV XENON, BOTTOM RIGHT) 5 KV XENON

TABLE 4.2: MEASURED AMORPHOUS LAYER THICKNESSES

| | 30 kV | 10 kV | 5 kV |
|---|---|---|---|
| Gallium | 60 nm | 27 nm | - |
| Xenon | 46 nm | - | 14 nm |

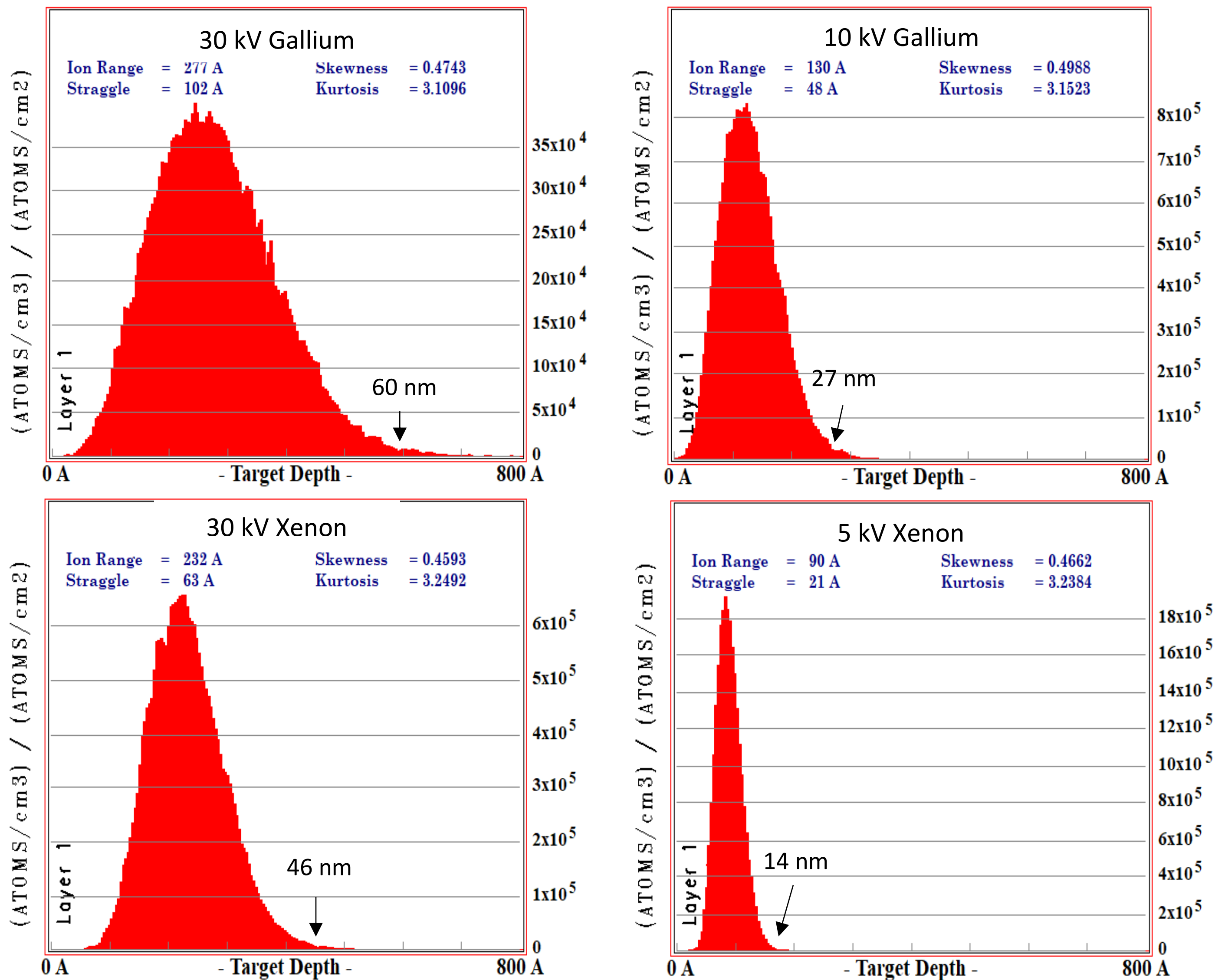


FIGURE 4.2: SRIM SIMULATIONS OF ION RANGE. TOP LEFT) GALLIUM 30 KV TOP RIGHT) GALLIUM 10 KV BOTTOM LEFT) XENON 30 KV BOTTOM RIGHT) XENON 5 KV

Though the median stopping range for both species was much smaller, the histograms show that at sufficient dose enough ions would penetrate deep enough to amorphize the full layer measured in the TEM. While only single samples were made of each beam setting, the thickness of the amorphous

layer was constant to within a few nanometers across the entire width of the samples and very close to the maximum penetration depth observed in SRIM simulations.

An additional phenomenon was apparent in the TEM images; that the implanted ions were not evenly distributed throughout the amorphous region. The most obvious example is the higher gallium concentration near the silicon surface; segregating into layers at the high dose setting (see fig 4.1, top), and as a smooth gradient at low dose settings (see Figure 4.3).

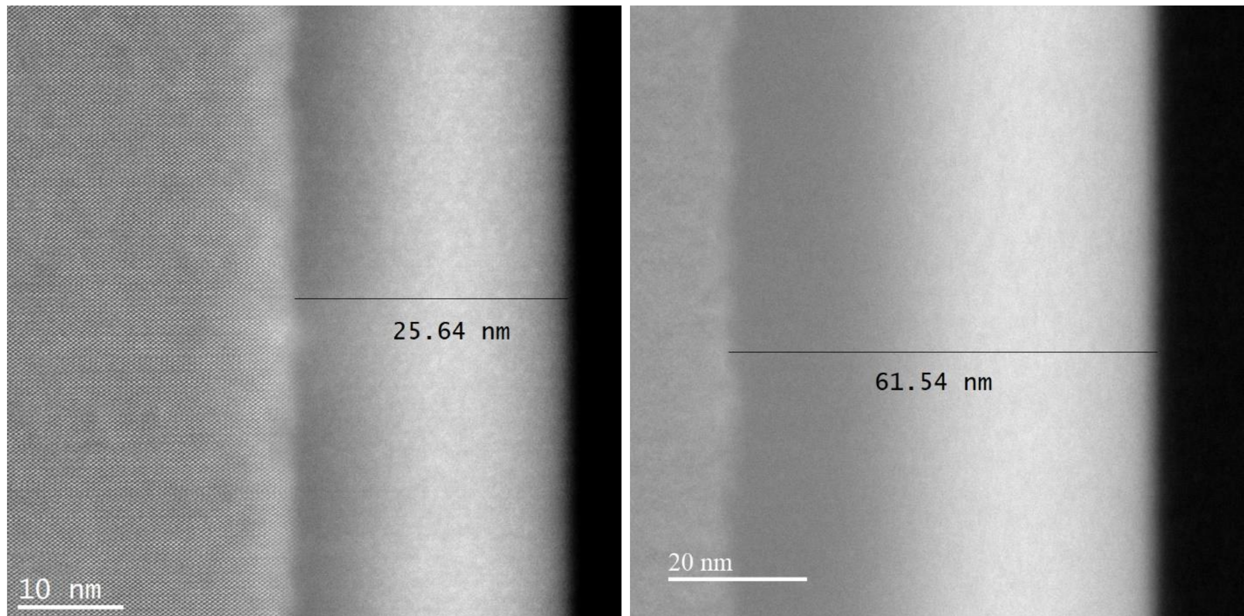


FIGURE 4.3: GALLIUM SEGREGATION AT LOW DOSE. LEFT) 10 KV, RIGHT) 30 KV

In xenon-dosed samples, the effect is also observed at both dose levels in the 5 kV samples and 30 kV samples, though less clearly. In contrast to the gallium samples, the clustering appears more homogenous throughout the amorphous zone, rather than toward the surface. EELS was used to confirm that the brighter areas in ADF images corresponded to a higher concentration of implanted beam ions (see Figure 4.4). The clustering and segregation effects in both sets of samples are likely related to the diffusion coefficient of each ion species in silicon, but more research is needed to elucidate this.

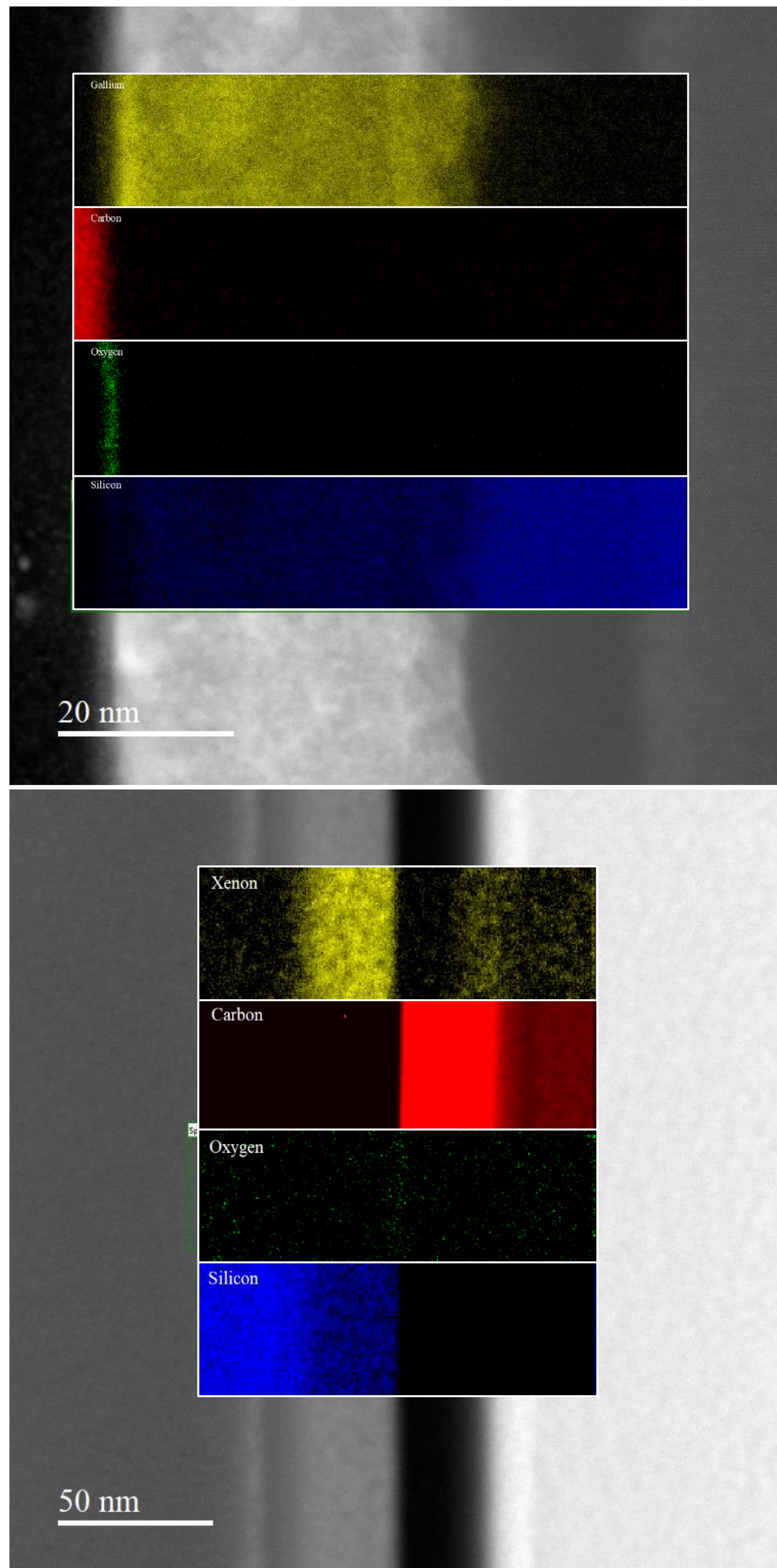


FIGURE 4.4: ADF IMAGE AND EELS MAPS OF HIGH-DOSE, 30 KV-IRRADIATED SAMPLES TOP) GALLIUM, BOTTOM) XENON

Finally, to understand the consequences of beam damage for optical coupling, Raman spectroscopy was used. In both gallium and xenon-exposed samples, the detected Raman intensity decreased significantly compared to unexposed areas (see Figure 4.5). Notably, however, there is no appearance of amorphous silicon's broad peak at 480 $cm^{-1}$. This suggests that the loss in signal is not

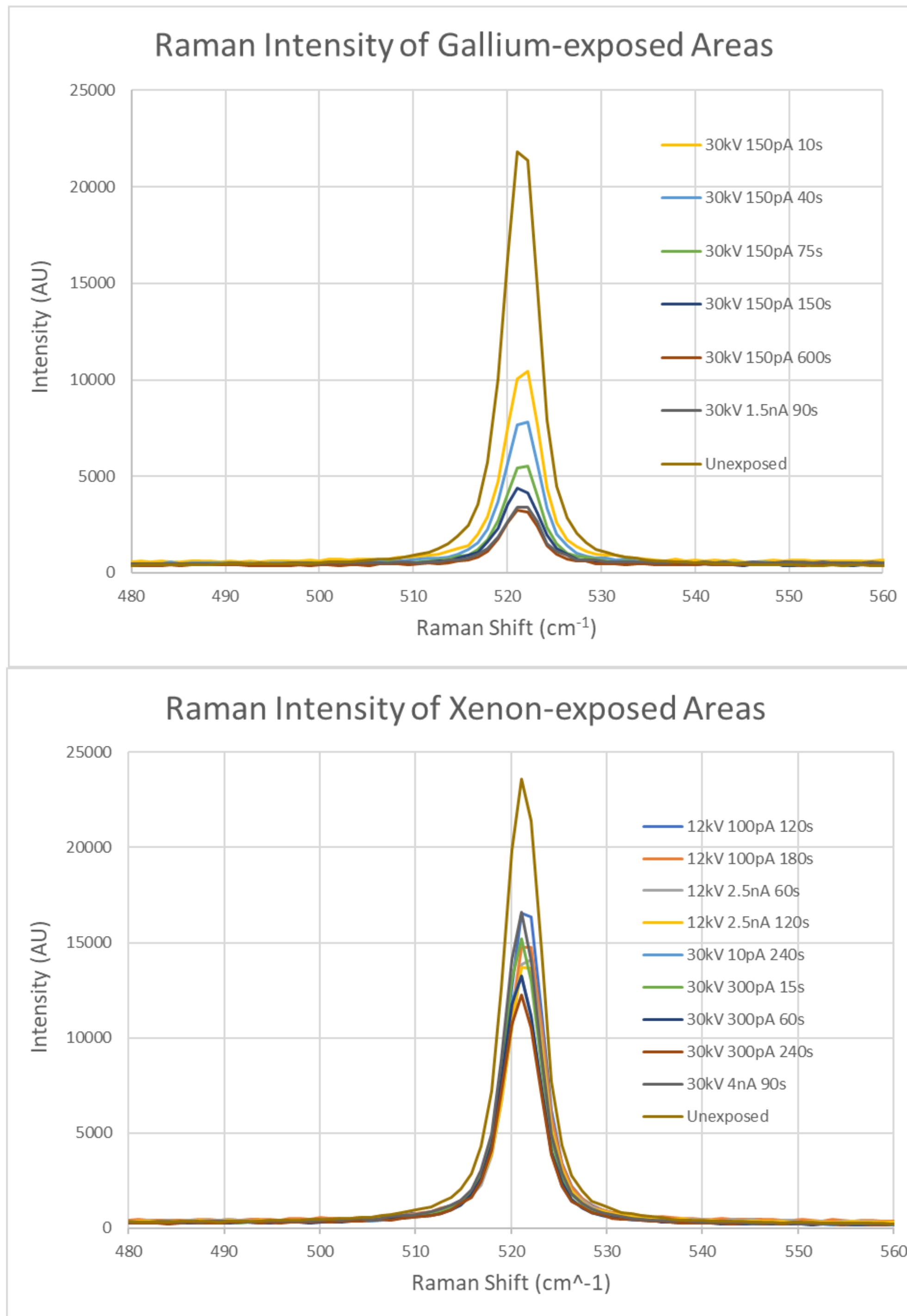


FIGURE 4.5: RAMAN SPECTRA OF GALLIUM AND XENON EXPOSED SILICON

caused by the amorphous layer of silicon absorbing the excitation light. Additionally, as seen in the SRIM modeling and TEM imaging, the amorphous layer from 30 kV xenon is about 23% thinner (46 nm versus 60 nm) than that of 30 kV gallium: unlikely to be solely responsible for the dramatic difference in optical loss – 37% in xenon compared to 80% in gallium, compared to undamaged silicon. Instead, this suggests that gallium specifically is harmful as a dopant species.

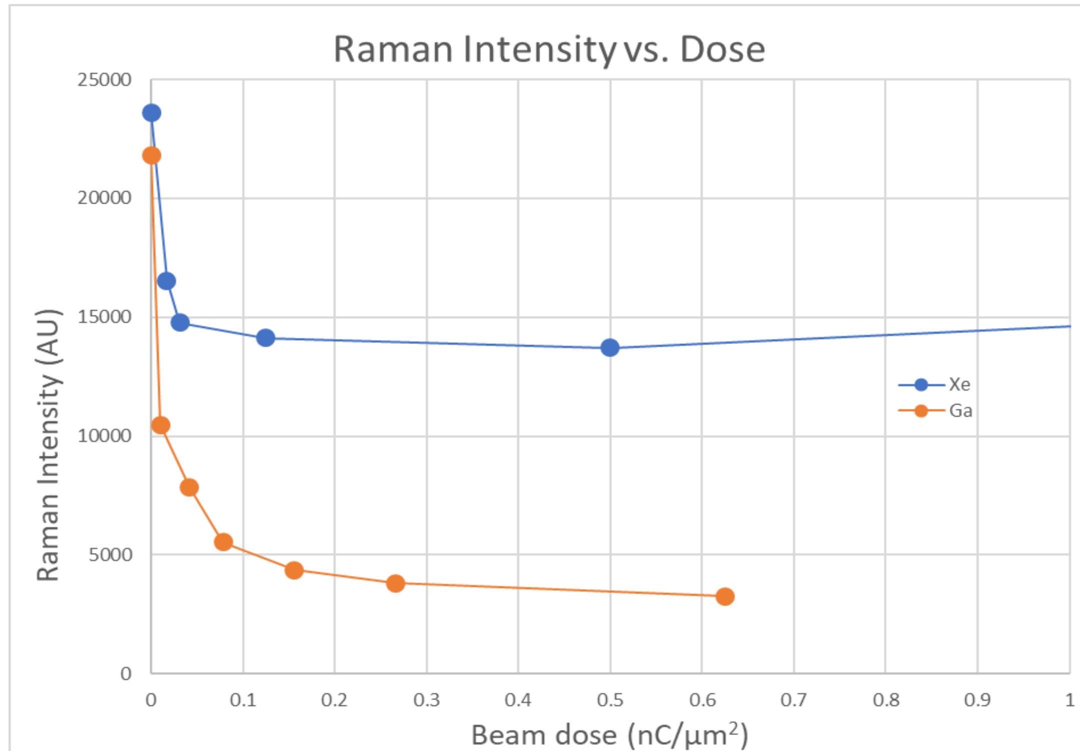


FIGURE 2: RAMAN INTENSITY VS ION DOSE FOR GA AND XE FIB (30 KV)

In Figure 4.6, Raman signal is plotted again ion dose, with lower y-values indicating less Raman coupling, and hence more optical damage. In both ion sources, the level of optical damage to the sample increases (Raman signal decreases) quickly at very low doses, but "saturates" at moderate doses (keep in mind that even the highest dose level of 0.625 nC/$\mu m^2$ is only sufficient to mill about 250 nm depth in silicon). This shows that gallium damage is more detrimental to optical coupling than xenon damage. The cause behind this is not fully understood. The nature of gallium clusters is highly dependent on at least several factors, including temperature gradient (dependent in turn on dose rate), substrate material, beam energy, and dose. In turn, a broad distribution of cluster size and concentration will lead to diverse optical absorption processes, many of which will not lead to emission of Raman-shifted light (Hole, Townsend, Barton, Nistor, & Van Landuyt, 1995). The differences between the low and high-dose gallium experiments shown above in TEM images (Figures 4.1 and 4.3) suggest a dynamic process – that

the distribution of gallium within the silicon matrix is not static, and that the mild segregation seen at low doses intensifies as exposure to the beam continues. In the 10 kV experiment beads of gallium were observed near the surface, similar to the beads seen in the IR polarizer (section 3.1.3). Clustering was also observed in some xenon-dosed samples; more study is needed to understand how the allowed optical processes in gallium and xenon clusters vary. A rigorous quantification of implanted concentration is also needed. A higher concentration of gallium in the lattice may be responsible for the degraded optical coupling.

# CHAPTER 5: CONCLUSIONS

Dualbeam FIB/SEM systems are versatile tools that today are found in most electron microscopy centers. Initially developed in the semiconductor industry for mask repair and circuit edit, FIB/SEM is now used for nanotomography, lithography, and especially APT and TEM sample preparation. The research included in this thesis was initially intended to utilize FIB/SEM's unique advantages (material-independence, direct-writing, and variable-depth milling) to develop fabrication methods for novel photonic devices. Devices were designed by collaborators at McMaster and other universities and included modified waveguides, DFB lasers, and chiral infrared polarizers in materials like silicon, indium phosphide, and hexagonal boron nitride. The designs were then fabricated in a gallium LMIS FIB and the optical performance of measured. In situations where the optical functionality was not highly dependent on surface integrity, the gallium FIB was found to be a useful tool. However, in other cases dependent on a monocrystalline substrate, performance was generally much lower than predicted by simulation. The cause of the poor performance was likely damage induced by the gallium ion beam, which has been documented in the literature (Chyr, Lee, Chao, & Steckl, 1999; Ridder, Hopman, & Ay, 2007). A xenon plasma-FIB was recently installed at McMaster, so the logical next step of this project was to compare damage from the gallium beam with damage from the xenon beam in hopes of using PFIB to fabricate devices that function as planned. To understand the differences between the ion sources, 12 µm x 12 µm areas of silicon wafer were exposed to a set amount of ion irradiation in both Ga and Xe FIBs and then characterized with Raman and TEM/EELS analysis. TEM is regarded as the gold standard in damage characterization because it can provide atomic resolution structural information; when used in conjunction with EELS spectroscopy, it can also provide high-resolution compositional and chemical information. The drawback of TEM/EELS is that the sample preparation process is expensive and time-

consuming. Raman spectroscopy on the other hand takes almost no sample preparation and useful data can be acquired in about 20 minutes, as opposed to more than a day. Raman directly evaluates the optical quality of the material by probing the integrity of the crystal structure.

By combining TEM and Raman analysis, it became clear that lattice amorphization was not the primary cause of optical losses – implanted beam ions are the primary contributor. This conclusion was drawn from several pieces of evidence. First, the difference in thickness of amorphous layer between the gallium and xenon sources is relatively small compared to the difference in Raman signal. Second, the Raman spectra show no peak from amorphous silicon, only a loss in intensity of the crystalline silicon peak. If a significant proportion of the Raman excitation light was being absorbed by amorphous silicon, the broad peak would be present. This not a surprise, since the penetration depth of the Raman lasers was much larger than the depth of the amorphous region in both samples. Third, though quantitative EELS was not done, a qualitative analysis of the EELS spectra does suggest a significantly higher concentration of implanted gallium compared to xenon.

This thesis fills a niche between the fields of optical devices and electron microscopy. There is little existing literature in this space. Most FIB damage studies related to TEM preparation leave out such factors as 30 kV and normal-incidence milling, and don't consider optical response when evaluating damage. Studies related to FIB for device fabrication are generally more concerned with device design and performance, and rarely pursue thorough characterization (Vallini, Barea, Reis, von Zuben, & Frateschi, 2012). There was only one study found in preparation of this work that characterized PFIB damage in any way, and it was limited to glancing angle TEM sample preparation (Kelley, Song, Van Leer, Wall, & Kwakman, 2013). With this research, future designers and fabricators can be more confident that FIB and PFIB-fabricated devices will function as expected.

## 5.1: FUTURE WORK

Several other ion sources are under development and promise to enter the marketplace in the near future such as cesium, lithium, neon, and others (Livengood et al., 2011; McClelland et al., 2016). The research included in this thesis shows that particular care must be taken when selecting an ion species to use for lithographic applications, particularly when the substrate material's optical properties must be maintained. The methods described above present a starting place on which to make that choice. Specifically, this research predicts the value of new xenon PFIBs for photonic device fabrication – an application that has been attempted using gallium FIBs with limited success. This project may be continued in several different directions. First is side-by-side fabrication and optical characterization of

devices with gallium and xenon FIBs in order to cement the relevance of this research. Ion-solid interactions from other recently developed sources may be characterized, as well as different damage phenomena in amorphous or composite material systems. Beam parameters such as dose rate may also have an influence. The collection of optical processes enabled by clustered implanted ions are not well understood, especially when ions form alloys or compounds with the matrix. Collectively, research of this variety is necessary to make educated guesses as to which nanofabrication projects are best suited to take advantage of FIB's capabilities.

# REFERENCES

Atwood, D. K., Fisanick, G. J., Johnson, W. A., & Wagner, A. (1984). *Defect Repair Techniques For X-Ray Masks* (Vol. 0471): SPIE.

Aydin, S., Carl, J. A., Philip, D. P., James, B., & Haider, B. (2015). Effects of current on early stages of focused ion beam nano-machining. *Materials Research Express, 2*(5), 055005.

Balasubramanian, K., Heard, P. J., & Cryan, M. J. (2006). Focused ion beam fabrication of two dimensional photonic crystals in silicon-on-insulator. *Journal of Vacuum Science & Technology B: Microelectronics and Nanometer Structures Processing, Measurement, and Phenomena, 24*(6), 2533-2537. doi:10.1116/1.2359729

Basov, D. N., Fogler, M. M., & García de Abajo, F. J. (2016). Polaritons in van der Waals materials. *Science, 354*(6309), aag1992. doi:10.1126/science.aag1992

Belz, J., Beyer, A., Torunski, T., Stolz, W., & Volz, K. (2016). Direct investigation of (sub-) surface preparation artifacts in GaAs based materials by FIB sectioning. *Ultramicroscopy, 163*, 19-30. doi:https://doi.org/10.1016/j.ultramic.2016.01.001

Bondi, A. (1964). van der Waals Volumes and Radii. *The Journal of Physical Chemistry, 68*(3), 441-451. doi:10.1021/j100785a001

Burnett, T. L., Winiarski, B., Kelley, R., Zhong, X. L., Boona, I. N., McComb, D. W., . . . Withers, P. J. (2016). Xe+ Plasma FIB: 3D Microstructures from Nanometers to Hundreds of Micrometers. *Microscopy Today, 24*(3), 32-39. doi:10.1017/S1551929516000316

Caldwell, J. D., Kretinin, A. V., Chen, Y., Giannini, V., Fogler, M. M., Francescato, Y., . . . Novoselov, K. S. (2014). Sub-diffractional volume-confined polaritons in the natural hyperbolic material hexagonal boron nitride. *Nature Communications, 5*, 5221. doi:10.1038/ncomms6221

https://www.nature.com/articles/ncomms6221#supplementary-information

Cantoni, M., & Holzer, L. (2014). Advances in 3D focused ion beam tomography. *MRS Bulletin, 39*(4), 354-360. doi:10.1557/mrs.2014.54

Chiu, P.-L., Li, X., Li, Z., Beckett, B., Brilot, A. F., Grigorieff, N., . . . Walz, T. (2015). Evaluation of super-resolution performance of the K2 electron-counting camera using 2D crystals of aquaporin-0. *Journal of Structural Biology, 192*(2), 163-173. doi:10.1016/j.jsb.2015.08.015

Chyr, I., Lee, B., Chao, L. C., & Steckl, A. J. (1999). Damage generation and removal in the Ga+ focused ion beam micromachining of GaN for photonic applications. *Journal of Vacuum Science & Technology B: Microelectronics and Nanometer Structures Processing, Measurement, and Phenomena, 17*(6), 3063-3067. doi:10.1116/1.590955

Cryan, M. J., Hill, M., Sanz, D. C., Ivanov, P. S., Heard, P. J., Tian, L., . . . Rorison, J. M. (2005). Focused ion beam-based fabrication of nanostructured photonic devices. *IEEE Journal of Selected Topics in Quantum Electronics, 11*(6), 1266-1277. doi:10.1109/JSTQE.2005.860990

CubeSatShop. (2019). IFM NanoThruster for CubeSats.
DeFreez, R. K. (1991). Focused-ion-beam micromachining: A fabrication tool for prototypal semiconductor lasers. *AIP Conference Proceedings, 227*(1), 92-95. doi:10.1063/1.40632
Deshpande, P., Vilayurganapathy, S., Bhat, K. N., & Ghosh, A. (2019). Study of Ga+ implantation in Si diodes: effect on optoelectronic properties using micro-spectroscopy. *Applied Physics A, 125*(3), 181. doi:10.1007/s00339-019-2467-2
Economou, N. P., Notte, J. A., & Thompson, W. B. (2012). The history and development of the helium ion microscope. *Scanning, 34*(2), 83-89. doi:10.1002/sca.20239
Fenn, J., Mann, M., Meng, C., Wong, S., & Whitehouse, C. (1989). Electrospray ionization for mass spectrometry of large biomolecules. *Science, 246*(4926), 64-71. doi:10.1126/science.2675315
Forbest, R. G. (1997). Understanding how the liquid-metal ion source works. *Vacuum, 48*(1), 85-97. doi:https://doi.org/10.1016/S0042-207X(96)00227-8
Giannuzzi, L. A., & Stevie, F. A. (1999). A review of focused ion beam milling techniques for TEM specimen preparation. *Micron, 30*(3), 197-204. doi:https://doi.org/10.1016/S0968-4328(99)00005-0
Glassbrenner, C. J., & Slack, G. A. (1964). Thermal Conductivity of Silicon and Germanium from 3\ifmmode^\circ\else\textdegree\fi{}K to the Melting Point. *Physical Review, 134*(4A), A1058-A1069. doi:10.1103/PhysRev.134.A1058
Halpin, J. E., Webster, R. W. H., Gardner, H., Moody, M. P., Bagot, P. A. J., & MacLaren, D. A. (2019). An in-situ approach for preparing atom probe tomography specimens by xenon plasma-focussed ion beam. *Ultramicroscopy, 202*, 121-127. doi:https://doi.org/10.1016/j.ultramic.2019.04.005
Harriott, L. R., Scotti, R. E., Cummings, K. D., & Ambrose, A. F. (1986). Micromachining of integrated optical structures. *Applied Physics Letters, 48*(25), 1704-1706. doi:10.1063/1.96809
Harriott, L. R., Wagner, A., & Fritz, F. (1986). Integrated circuit repair using focused ion beam milling. *Journal of Vacuum Science & Technology B: Microelectronics Processing and Phenomena, 4*(1), 181-184. doi:10.1116/1.583433
Hillier, J., & Baker, R. F. (1944). Microanalysis by Means of Electrons. *Journal of Applied Physics, 15*(9), 663-675. doi:10.1063/1.1707491
Hole, D. E., Townsend, P. D., Barton, J. D., Nistor, L. C., & Van Landuyt, J. (1995). Gallium colloid formation during ion implantation of glass. *Journal of Non-Crystalline Solids, 180*(2), 266-274. doi:https://doi.org/10.1016/0022-3093(94)00477-3
Inkson, B. J., Mulvihill, M., & Möbus, G. (2001). 3D determination of grain shape in a FeAl-based nanocomposite by 3D FIB tomography. *Scripta Materialia, 45*(7), 753-758. doi:https://doi.org/10.1016/S1359-6462(01)01090-9
Ivo Utke, S. M., Phillip Russell. (2012). *Nanofabrication Using Focused Ion and Electron Beams*.
Kato, N. I., Kohno, Y., & Saka, H. (1999). Side-wall damage in a transmission electron microscopy specimen of crystalline Si prepared by focused ion beam etching. *Journal of Vacuum Science & Technology A, 17*(4), 1201-1204. doi:10.1116/1.581795
Kelley, R. D., Song, K., Van Leer, B., Wall, D., & Kwakman, L. (2013). Xe+ FIB Milling and Measurement of Amorphous Silicon Damage. *Microscopy and Microanalysis, 19*(S2), 862-863. doi:10.1017/S1431927613006302
Komuro, M., Kanayama, T., Hiroshima, H., & Tanoue, H. (1983). Measurement of virtual crossover in liquid gallium ion source. *Applied Physics Letters, 42*(10), 908-910. doi:10.1063/1.93784
Kudriavtsev, Y., Villegas, A., Godines, A., & Asomoza, R. (2005). Calculation of the surface binding energy for ion sputtered particles. *Applied Surface Science, 239*(3-4), 273-278. doi:10.1016/j.apsusc.2004.06.014
Larson, D. J., Foord, D. T., Petford-Long, A. K., Anthony, T. C., Rozdilsky, I. M., Cerezo, A., & Smith, G. W. D. (1998). Focused ion-beam milling for field-ion specimen preparation:: preliminary

investigations. *Ultramicroscopy, 75*(3), 147-159. doi:https://doi.org/10.1016/S0304-3991(98)00058-8

Li, C., Habler, G., Baldwin, L. C., & Abart, R. (2018). An improved FIB sample preparation technique for site-specific plan-view specimens: A new cutting geometry. *Ultramicroscopy, 184*, 310-317. doi:https://doi.org/10.1016/j.ultramic.2017.09.011

Livengood, R. H., Tan, S., Hallstein, R., Notte, J., McVey, S., & Faridur Rahman, F. H. M. (2011). The neon gas field ion source—a first characterization of neon nanomachining properties. *Nuclear Instruments and Methods in Physics Research Section A: Accelerators, Spectrometers, Detectors and Associated Equipment, 645*(1), 136-140. doi:https://doi.org/10.1016/j.nima.2010.12.220

McCaffrey, J. P., Phaneuf, M. W., & Madsen, L. D. (2001). Surface damage formation during ion-beam thinning of samples for transmission electron microscopy. *Ultramicroscopy, 87*(3), 97-104. doi:http://dx.doi.org/10.1016/S0304-3991(00)00096-6

McClelland, J. J., Steele, A. V., Knuffman, B., Twedt, K. A., Schwarzkopf, A., & Wilson, T. M. (2016). Bright focused ion beam sources based on laser-cooled atoms. *Applied Physics Reviews, 3*(1), 011302. doi:10.1063/1.4944491

Melngailis, J. (1987). FOCUSED ION-BEAM TECHNOLOGY AND APPLICATIONS. *Journal of Vacuum Science & Technology B, 5*(2), 469-495. doi:10.1116/1.583937

Müller, E. W., & Bahadur, K. (1956). Field Ionization of Gases at a Metal Surface and the Resolution of the Field Ion Microscope. *Physical Review, 102*(3), 624-631. doi:10.1103/PhysRev.102.624

Orloff, J. (1993). High-resolution focused ion beams. *Review of Scientific Instruments, 64*(5), 1105-1130. doi:10.1063/1.1144104

Overwijk, M. H. F., Heuvel, F. C. v. d., & Bulle-Lieuwma, C. W. T. (1993). Novel scheme for the preparation of transmission electron microscopy specimens with a focused ion beam. *Journal of Vacuum Science & Technology B: Microelectronics and Nanometer Structures Processing, Measurement, and Phenomena, 11*(6), 2021-2024. doi:10.1116/1.586537

Pendry, J. B. (2000). Negative Refraction Makes a Perfect Lens. *Physical Review Letters, 85*(18), 3966-3969.

Ridder, R. M. d., Hopman, W. C. L., & Ay, F. (2007, 1-5 July 2007). *Focused-Ion-Beam Processing for Photonics.* Paper presented at the 2007 9th International Conference on Transparent Optical Networks.

Smith, D. R., Pendry, J. B., & Wiltshire, M. C. K. (2004). Metamaterials and Negative Refractive Index. *Science, 305*(5685), 788-792. doi:10.1126/science.1096796

Smith, N. S., Tesch, P. P., Martin, N. P., & Kinion, D. E. (2008). A high brightness source for nano-probe secondary ion mass spectrometry. *Applied Surface Science, 255*(4), 1606-1609. doi:https://doi.org/10.1016/j.apsusc.2008.05.141

Swanson, L. W. (1983). Liquid metal ion sources: Mechanism and applications. *Nuclear Instruments and Methods in Physics Research, 218*(1), 347-353. doi:https://doi.org/10.1016/0167-5087(83)91005-0

Thorlabs. (2015). Spec Sheet, 1550 nm, 2mW, Pigtailed DFB Laser Diode.

Uberoi, M. S. (1964). <strong>Ion Propulsion for Space Flight.</strong> Ernst Stuhlinger. McGraw-Hill, New York, 1964. xviii + 373 pp. Illus. $17.50. *Science, 145*(3636), 1037-1038. doi:10.1126/science.145.3636.1037-a

Vallini, F., Barea, L. A. M., Reis, E. F. d., von Zuben, A. A., & Frateschi, N. C. (2012). Induced Optical Losses in Optoelectronic Devices due to Focused Ion Beam Damages. *arXiv preprint arXiv:1207.2359*.

Wang, V., Ward, J. W., & Seliger, R. L. (1981). A mass-separating focused-ion-beam system for maskless ion implantation. *Journal of Vacuum Science and Technology, 19*(4), 1158-1163. doi:10.1116/1.571234

Williams, J. (2014). The Dual-Beam—Its Birth, Progress, And Future. *Microscopy Today, 22*.

Zhou, Z., Yin, B., & Michel, J. (2015). On-chip light sources for silicon photonics. *Light: Science &Amp; Applications, 4*, e358. doi:10.1038/lsa.2015.131

Ziegler, J. F. B., J. P.; Ziegler M. D. (2008). *SRIM - The Stopping and Range of Ions in Matter*. New York: SRIM Co.